Supporting Information

Source quantification of South Asian black carbon aerosols with isotopes and modeling

*Sanjeev Dasari[1], August Andersson[1], Andreas Stohl[2#], Nikolaos Evangeliou[2], Srinivas Bikkina[1¤], Henry Holmstrand[1], Krishnakant Budhavant[1,3,4], Abdus Salam[5], and Örjan Gustafsson[1]**

[1]Department of Environmental Science, and the Bolin Centre for Climate Research, Stockholm University, Stockholm 10691, Sweden

[2]Norwegian Institute for Air Research (NILU), Kjeller 2027, Norway

[3]Maldives Climate Observatory at Hanimaadhoo (MCOH), Maldives Meteorological Services, Hanimaadhoo 02020, Republic of the Maldives

[4]Divecha Centre for Climate Change, Indian Institute of Science, Bangalore 560012, India

[5]Department of Chemistry, University of Dhaka, Dhaka 1000, Bangladesh

Current address: [#]Department of Meteorology and Geophysics, University of Vienna, Vienna 1010, Austria

[¤]Chubu Institute for Advanced Studies, Chubu University, Kasugai 487 8501, Japan

*Corresponding Author: Phone: +46 70 324 73 17; E-mail: orjan.gustafsson@aces.su.se

Supporting information includes: 44 pages, 7 Notes, 13 Figures, and 9 tables

Contents

Supplementary Notes

Note S1. A discussion on the radiocarbon ($\Delta^{14}C$) isotope endmember for biomass burning, based on trends in atmospheric $^{14}CO_2$

Fresh Biomass: A long-term decreasing trend in contemporary $\Delta^{14}C$-CO_2 has been observed over pristine sites in northern and southern latitudes after the *post-bomb period*[1-3]. Based on observations from the southern hemisphere, the $\Delta^{14}C$-CO_2 during 2015-2016 was ~ +20‰[3]. This value also coincides with the observations from a northern mid-latitude site (upon assuming a steady annual decrease of roughly 3‰ since 2012)[1-3]. It has been suggested that for tropical regions an additional 5‰ increase in $\Delta^{14}C$-CO_2 is plausible due to the increasing fossil fuel CO_2 emissions in the northern mid-latitudes which increases the meridional gradient and thereby the background in the tropics[1]. This aspect was taken into consideration based on the northern and southern hemispherical values for $\Delta^{14}C$-CO_2. Thus, the $\Delta^{14}C$-CO_2 for contemporary biomass (meaning one-year plants) for the South Asian region was approximated to be +20±10‰ as of year 2016.

Aged Biomass: The $\Delta^{14}C$ value for multi-year biomass sources are complicated by the atmospheric nuclear bomb tests in the 1960s, which significantly increased the ^{14}C levels in CO_2 at that time. Although these enriched levels are also decreasing on decadal time-scales, this means that the $\Delta^{14}C$ signature of a tree is essentially dependent on when/for how long it was growing, and the annual increase in biomass[1-5]. Hence, trees with life-span on the order of 100 years, will have accumulated $\Delta^{14}C$ signature non-linearly over this time which in general is ~ less than half the age of the tree[4,5]. On the other hand, one-year plants will only represent the atmospheric ^{14}C signature of CO_2 for that year[4]. This complicates the situation as a few assumptions regarding the non-linear biomass accumulation of over time need to be made. Moreover, the age of the trees is region specific and hence the distribution of tree ages is different for different regions of the world (temperate vs. non-temperate)[4,6].

To test the dependency of the biomass age and the $\Delta^{14}C$ signature we made a sensitivity analysis. Although very few trees in South Asia are > 100 years[6] , initially, we assume that biomass was uniformly distributed in trees between 1800 to 2015. This would mean averaging over the entire $^{14}CO_2$ curve[5] including the period of the *bomb-spike*. This leads to a $\Delta^{14}C$ endmember of +108±50‰. By reducing the biomass age and averaging from 1900 to 2015 we get +132±57‰ ; 1950 to 2015 we get +126±70‰ ; 1980 to 2015 we get +119±71‰. Hence, the overall average for 215-year age of biomass vs. 35-year age of biomass are overlapping. By comparison, this endmember (+108±50‰) was similar to wood smoke endmember value (+107.5‰) from the tree growth model derived by averaging $\Delta^{14}C$ values for 10 to 85-year old wood fractions as well[7,5]. In addition, this $\Delta^{14}C$ endmember (+108±50‰)

value was also found to be similar to the endmember value from wood smoke (+102.5‰) derived from averaging sections of an 80-year-old pinewood in an indoor study[7]. A $\Delta^{14}C$ endmember (+107.5±50‰) from wood burning in temperate regions was also found to be close to the estimated value from the sensitivity test[8]. Thus, based on the observations[5,7,8] and the sensitivity measure we approximated the $\Delta^{14}C$ endmember for wood logged in the late 1990s and 2000s (~ 20 to 30-year aged biomass) to be +110±70‰.

Note S2. South Asia-specific radiocarbon biomass endmember ($\Delta^{14}C_{biomass}$)

For South Asia we consider two main biomass combustion sources: C_3-plants (the largest group of terrestrial plants e.g., wood, rice, wheat), C_4-plants (e.g., sugarcane, maize, millet). This division is based on two principles: i) These source categories together capture most emissions of BC biomass in South Asia[9] and, ii) These sources may be differentiated by using dual-carbon isotope techniques[10,11].

Based on emission estimates of biomass burning from South Asian black carbon emission inventories[9], we estimated the weighted contribution of C_3- and C_4-plants in various sectors: Crop residue burning (50% C_3 + 50% C_4); Forest Fire (100% C_3); Garbage burning (100% C_3 ; 50% biomass overall); Dung cake (100% C_3); Agricultural residue (50% C_3 + 50% C_4) and Firewood (100% C_3). Combining the weighted average of biomass emissions from these sectors, we computed the weighted $\Delta^{14}C_{biomass}$ endmember. The $\Delta^{14}C_{C3}$ endmember is approximated to be +77±60‰. The $\Delta^{14}C_{C4}$ endmember is approximated to be +20±10‰ (see Note S1). The South Asia-specific $\Delta^{14}C_{biomass}$ endmember is thus approximated to be +70±35‰. The computation is provided in SI Table S8.

Note S3. Isotopic fractionation in the biomass source classes

The biomass sources can be divided into two categories based on photosynthetic pathways leading to distinct stable isotopic signatures: C_3-plants are named based on the three-carbon compound produced by the CO_2 fixation mechanism[10]. The CO_2 uptake in this category of plants is limited by the carboxylation step involving large fractionation (~20‰) causing the average $\delta^{13}C_{C3}$ biomass to cluster around -27.1±2.0‰[10]. The C_4-plants produce a four-carbon compound in a more efficient form of CO_2 fixation. The rate limiting step is suggested to be diffusion rather than carboxylation involving a relatively smaller isotopic fractionation (~ 4‰). Thus, the average $\delta^{13}C_{C4}$ biomass has been reported to cluster around -13.1± 1.2‰[10]. Other, presumably less important, factors which contribute to the variability within the $\delta^{13}C$ range of C_3- and C_4 biomass include species, latitude/longitude, soil water deficit, irradiance, topographic position, degree of utilization of respired CO_2[10,12,13].

Combustion of C_3- and C_4 biomass may induce carbon isotopic fractionation. Both plant type (e.g., initial starting material) and burn conditions (e.g., temperature, humidity and ventilation) have been shown to modulate the fractionation effects[12,13]. The differences in the biochemical fractions of depleted (e.g., lignin, cellulose, lipids) vs enriched (hemicellulose, sugars) compounds in the plant material or differences in the isotopically distinct component diverted to or retained during burning has been reported to affect the magnitude of fractionation[12,13].

Several field and chamber investigations of aerosol (smoke) and residue (ash) from biomass burning have revealed that the C_3-plants generally do not significantly fractionate C isotopes (< 0.7‰), implying that BC produced from burning C_3 biomass usually represents the $\delta^{13}C$ of the original plant[12,13]. However, the C_4-plants have shown to have a plant-specific fractionation (C-13 depletion) ranging from 0.5‰ to 7‰[10,12,13]. As an example, the isotopic fractionation in indoor burn experiments for sugarcane has yielded only a slight isotopic fractionation (< 1‰) compared to other C_4-type grasses which have shown substantial depletion of ~ 4‰ and higher relative to the original plant material[12]. As the major fraction of crop-residue burnt in South Asia is C_3-type followed by C_4 (mostly sugarcane)[14], the isotopic fractionation effects during biomass burning are considered insignificant for these biomass types in South Asia and hence the $\delta^{13}C_{BC}$ endmembers for both these categories are assumed to be the same as the original plant material (see SI Table S5 for isotopic endmembers).

Note S4. A discussion on the sample SPX-BHL-121 not used in source apportionment calculations

The sample SPX-BHL-121 was collected between 23rd Jan 2016 (5:00 pm) – 24th Jan 2016 (8:00 am). The sampling parameters from DH-77 Hi-vol sampler (flow rate- 520 l/min, frequency- 141, V_a-461m^3) showed no peculiarity. Further, the OC, EC and IC data were comparable to other samples collected from BCOB during SAPOEX-16. The HYSPLIT based back-trajectories also showed the IGP influence similar to other samples collected during January 2016.

The EC (BC)-isotopic data reported in SI Table S4 for sample SPX-BHL-121 (accession #: OS-141179) was found to be ambiguous. SPX-BHL-121 was isolated for EC-isotopic investigation twice during Batch-1 submission of samples owing to poor recovery in the first run (accession #: OS-137341; 24% recovery; $\delta^{13}C$: -29.05; $\Delta^{14}C$: -398). While the sample was isolated again, it was mislabeled as SPX-MCOH-39 (accession #: OS-137420; 74% recovery; $\delta^{13}C$: -29.05; $\Delta^{14}C$: -752.93) and sent to NOSAMS.

Owing to this discrepancy, SPX-BHL-121 sample was isolated for CO_2 for a third time and submitted as SPX-BHL-5 (accession #: OS-141179) during Batch-2 submission in late April 2018. The result from Batch-2 is provided in SI Table S4 (accession #: OS-141179; 94% recovery; $\delta^{13}C$: -31.49; $\Delta^{14}C$: -988.26).

Possible reasons for ambiguity:

Human error: It is possible that the filter punches of SPX-BHL-121 (accession #: OS-137341, 137420) were mistakenly combined with filter punches of the sample SPX-MCOH-39 which was kept in another petri dish. SPX-MCOH-39 was eventually not cryo-trapped for isotopic investigation. The punches were only used to check EC concentrations and split time. As the EC concentrations turned out to be lower than most of the SPX-MCOH samples, this sample was not used in cryo-trapping and 2 filter punches of 1.5 cm^2 each were left over in the respective petri dish. Although filter punches from each sample were segregated into individual petri dishes and labelled during analysis with extreme care and precaution, the aspect of human error cannot be neglected. The possible influence of mixed filter punches could have caused SPX-BHL-121 (accession #: OS-137341, accession #: OS-137420) to have a completely different $\Delta^{14}C/\delta^{13}C$ signature than the third-run isotopic investigations of SPX-BHL-121 (accession #: OS-141179).

Local emission: BCOB is a rural site with limited activity around the observatory and receives aerosols predominantly from the IGP region during winter (SI Figures S2-S3). Assuming the third-run isolate of SPX-BHL-121 (accession #: OS-141179) is devoid of the aspect of human error, based on

the $\Delta^{14}C$ values showing a highly depleted (> 90% fossil) signature, it is plausible that the sample is affected by emissions from ^{13}C depleted fuels like natural gas. However, gas-flaring is not a common source of black carbon emissions in South Asia[15,16]. It is possible that there could be an affect from a steamer/cruise ship (running on natural gas) crossing the region in the N. Bay of Bengal. A combination of extremely low wind speeds and stable boundary layer might cause the BCOB footprint to be potentially affected by such an event.

Overall, SPX-BHL-121 has shown large fluctuations in the isotopic signatures and the reasons for these are still unclear. Owing to the uncertainty, we have not included this data in further source apportionment calculations in the current manuscript.

Note S5. Bayesian statistical modeling for SAPOEX-16 study

By combining the dual isotope signatures ($\Delta^{14}C$ and $\delta^{13}C$) and assuming mass balance, it is possible to differentiate the relative contributions from various source classes (SCs):

$$\begin{Bmatrix} \Delta^{14}C_{sample} \\ \delta^{13}C_{sample} \\ 1 \end{Bmatrix} = \begin{pmatrix} \Delta^{14}C_{SC\,1} & \Delta^{14}C_{SC\,2} & \Delta^{14}C_{SC\,3} & \Delta^{14}C_{SC\,4} \dots \\ \delta^{13}C_{SC\,1} & \delta^{13}C_{SC\,2} & \delta^{13}C_{SC\,3} & \delta^{13}C_{SC\,4} \dots \\ 1 & 1 & 1 & 1 \quad \dots \end{pmatrix} \begin{Bmatrix} f_{SC\,1} \\ f_{SC\,2} \\ f_{SC\,3} \\ f_{SC\,4} \\ \dots \end{Bmatrix} \quad (1)$$

A major complication to solving Equation 1 for realistic applications is the variability in the isotopic signatures of $\Delta^{14}C$ and $\delta^{13}C$ of various source classes i.e., endmember variability (e.g., SI Table S5). For $\Delta^{14}C$, the fossil source is completely depleted in ^{14}C ($\Delta^{14}C$ = -1000±0‰), the endmember variability thus relates to biomass. For SAPOEX-16, based on weighted black carbon emissions from C_3- and C_4-biomass source classes, we established a South Asia specific biomass endmember $\Delta^{14}C_{biomass}$ = +70±35‰ (SI Notes S1-S2 and Table S8). For $\delta^{13}C$, the endmember variability is larger and less well-constrained, due limited in-source measurements. The $\delta^{13}C$ endmembers used in this study are based on a thorough literature review of existing $\delta^{13}C$ data for C_3- and C_4-biomass source classes (SI Note S3 and Table S5) and from our previous publication where the liquid fossil and fossil coal $\delta^{13}C$ endmembers were established[11]. As this data is reported in different formats (individual data points; ranges; and mean ± standard deviation) a careful statistical assessment for each source class category was made and then the following endmember values were established: $\delta^{13}C_{coal}$= -23.4±1.3‰, $\delta^{13}C_{liquid\ fossil}$= -25.5±1.3‰, $\delta^{13}C_{C3\text{-}biomass}$= -27.1±2‰, $\delta^{13}C_{C4\text{-}biomass}$= -13.1±1.2‰. The uncertainties in endmembers dominate over the measurement uncertainties. The narrow variability of our $\delta^{13}C$ and $\Delta^{14}C$ data for a given site/month, also suggests this to be the case (SI Tables S4-S5).

It is recognized that in order to correctly estimate the relative source contributions and related uncertainties, the endmember variability as well as other sources of uncertainty needs to be included in the analysis[17-19]. Markov Chain Monte Carlo (MCMC)-driven Bayesian approaches have recently been implemented to account for multiple sources of uncertainties/variabilities. Such an approach for isotope-based source apportionment of atmopsheric aerosols was recently established in a previous publication[11] and has been used in multiple studies[15,18,20-22]. Given the authenticity of the $\delta^{13}C$ endmember distributions and the underlying well-established statistical methodology, the resulting estimates of the relative source contributions are very robust; the resulting probability density functions therefore give a 'least-biased' representation of the precision.

For SAPOEX-16, we have simulated 3 different MCMC scenarios: i) The under-determined system with C_3 biomass, C_4 biomass, liquid fossil, and fossil coal; $MCMC_4$, ii) The determined system with C_3 biomass, liquid fossil, and fossil coal; $MCMC_{3,coal}$ (all but no C_4-biomass), iii) The determined system with C_3 biomass, C_4 biomass, and liquid fossil; $MCMC_{3,C4}$ (all but no fossil coal). For the under-determined scenario, we have an isotopic mass-balance as:

$$\begin{Bmatrix} \Delta^{14}C_{sample} \\ \delta^{13}C_{sample} \\ 1 \end{Bmatrix} = \begin{Bmatrix} \Delta^{14}C_{C3} & \Delta^{14}C_{C4} & \Delta^{14}C_{liq.fossil} & \Delta^{14}C_{fossil\ coal} \\ \delta^{13}C_{C3} & \delta^{13}C_{C4} & \delta^{13}C_{liq.fossil} & \delta^{13}C_{fossil\ coal} \\ 1 & 1 & 1 & 1 \end{Bmatrix} \begin{Bmatrix} f_{C3} \\ f_{C4} \\ f_{liq.fossil} \\ f_{fossil\ coal} \end{Bmatrix} \quad (2)$$

For the determined scenario (as an example $MCMC_{3,coal}$), we have an isotopic mass-balance as:

$$\begin{Bmatrix} \Delta^{14}C_{sample} \\ \delta^{13}C_{sample} \\ 1 \end{Bmatrix} = \begin{Bmatrix} \Delta^{14}C_{C3} & \Delta^{14}C_{liq.fossil} & \Delta^{14}C_{fossil\ coal} \\ \delta^{13}C_{C3} & \delta^{13}C_{liq.fossil} & \delta^{13}C_{fossil\ coal} \\ 1 & 1 & 1 \end{Bmatrix} \begin{Bmatrix} f_{C3} \\ f_{liq.fossil} \\ f_{fossil\ coal} \end{Bmatrix} \quad (3)$$

Where f denotes the fractional contribution from a given source, sample denotes the value of the analyzed field sample and the other isotope-values are source signatures ('C_3', 'C_4', 'liq. fossil', and 'coal' corresponding to C_3 biomass, C_4 biomass, liquid fossil fuel, and fossil coal respectively; See SI Tables S4-S5). The key difference in these scenarios is the number of sources that are used in the source apportionment calculation as well as the type of sources considered. The observed dual-isotope signatures are then apportioned relative to the endmembers of each of these sources (SI Table S5). Hence, based on the geometry of the data with respect to the endmembers in each of these scenarios, the contribution of the sources in expected to differ. The *posterior* probability density functions of relative source contributions for the source apportionment conducted using these three MCMC scenarios for SAPOEX-16 is presented in SI Figure S5.

Note S6. FLEXPART-ECLIPSE-GFED modeling for SAPOEX-16 study

For the bottom-up estimates of BC concentrations at MCOH the Lagrangian particle dispersion model FLEXPART version 9.2[23,24] was used. A particular advantage of FLEXPART over ordinary air mass back-trajectory models is that it involves many processes relevant for removal as well as dispersion of aerosols such as wet and dry deposition, convective mixing, turbulence above and below the boundary layer[23]. Furthermore, FLEXPART can be run in two in-time modes: forward and backward. With forward modeling, concentration fields are simulated whereas backward modeling (typically initialized from a measurement location i.e., receptor point) provides source-receptor relationships, also referred to as potential emission sensitivity (PES)[25]. The PES describes the sensitivity of receptor 'z' to source 's'. A matrix with elements $\frac{z}{s}$ forms the source-receptor relation. The backward modeling is useful to understand contributing source regions and transport pathways to the observation site.

For simulations during SAPOEX-16, we conducted backward runs with MCOH as a receptor point. The receptor 'z' is then a vector of 48h BC measurements at MCOH for the entire sampling period and 's' is vector of area-averaged BC emissions in different grid-boxes at different time intervals. A logarithmic size distribution with a mean particulate diameter of 250 nm (aerodynamic diameter) particle density of 1500 kg m^{-3} and variation of sigma 0.3 (logarithmic S.D.) was used to calculate dry deposition[26]. Below-cloud scavenging[26] was enabled using set values of wet scavenging coefficient ($A=2*10^{-7}$ s^{-1}), precipitation rate (I= 1 mm hr^{-1}) and factor dependency (B= 0.62) using the relation $A*I^B$. In-cloud scavenging was enabled using scavenging coefficient defined as $(1.25 * I^{0.64})* H^{-1}$ where H is the cloud thickness in metres[27]. The simulations used meteorological analysis data from the European Centre for Medium-Range Weather Forecasts (ECMWF) at a resolution of 1º x 1º latitude/longitude. Backward runs extended over 20 days back in time, which is enough to include most emissions injected into an air mass arriving at the station, given a typical BC lifetime on the order of a week.

For anthropogenic BC emission information, FLEXPART was coupled to the emission inventory ECLIPSE (Evaluating the climate and air quality impacts of short-lived pollutants; version 5 baseline scenario for the year 2010)[16], which is developed using the GAINS model (Greenhouse gas - Air pollution Interactions and Synergies)[28]. The ECLIPSE emission data set extends to 2010 and baseline projections till 2050 is based on the IEA – International Energy Agency's Energy Technology Perspective 2012 (ETP 2012)[29,30]. The emissions are available on a yearly resolution (from which monthly are derived by splitting into 12 components) for various source types such as residential combustion, transport and shipping, thermal plants. Version 5 has ~44% higher emissions over India

than version 4a as regional sources such as wick lamps and diesel generators have been included[16]. For this study, the emissions were explicitly split between biofuel (modern; for example, wood burning) and fossil fuel emissions (SI Tables S6 and S9). This customization enabled direct comparison of modeled results with source-segregated observations (Figure 4 in the main manuscript). Uncertainty estimates related to individual emissions are not available for GAINS.

Open biomass burning BC emissions, from vegetation fires and agricultural waste burning, were received from the Global Fire Emissions Database (GFED) version 4.1s[31]. Monthly temporal and 0.5º spatial resolutions were used for GFED inventory as well. Emissions from agricultural waste burning included in ECLIPSE as biofuel was not used in order to avoid double counting, because these were included in GFED. The 4.1s version which is an upgrade from previous versions GFED3 and GFED4, includes burned area from small fires (hence the suffix "s")[31-33]. The burned area is derived from MODIS (Moderate Resolution Imaging Spectroradiometer) Collection 5.1, MCD64A1 product with a 500m spatial resolution. This is combined with 1km thermal anomalies detected on board MODIS Terra and Aqua satellite and 500m surface reflectance observations, to statistically estimate burned area for small fires. The total emissions from open fires in GFED is then derived from the multiplication of the total burned area and fuel consumption per unit burned area[31]. The dry matter burned are converted to emissions of trace gases and aerosols using a set of high-resolution emission factors provided in GFED as well[34].

Note S7. Air mass back trajectories and identification of source regions for SAPOEX-16 study

The NOAA Hybrid Single-Particle Lagrangian Integrated Trajectory model (HYSPLIT) version 4[35] was used to generate five-day air mass back trajectories (BTs) for BCOB and nine-day BTs for MCOH using the Global Data Assimilation System (GDAS; 1º × 1º) archived dataset, respectively. The BTs were generated at an arrival height of 100 m for every 3 h. This was followed by detailed air mass cluster analysis using the HYSPLIT desktop-based software (See SI Figure S2). The following air mass clusters were deduced; (a) At BCOB – i) IGP, ii) N Bay of Bengal (N BOB; passing over the eastern coast of India), (b) At MCOH – i) IGP [and passing over N BOB] , ii) SE Asia [and passing over S BOB and peninsular India], iii) Central Arabian Sea (including peninsular India), iv) Eastern Arabian Sea (including western Indian margin). Clusters iii and iv were clubbed to form a single cluster Arabian Sea (ARS).

To further ascertain the influence of air mass clusters to the aerosol sampling conducted at both sites, the fractional cluster contribution (for every 24h) was computed for the entire duration of the campaign (SI Figure S3 a-b). Overall, it is clear that there was a temporal shift in the meteorology causing air masses from different source regions to be intercepted at BCOB and MCOH during SAPOEX-16. Although this analysis provides quantitative apportionment of the clusters, it is not fully effective in delineating the potential contribution of various source regions to the observed aerosol concentrations at both sites. We, therefore, performed the concentrated weighted trajectory (CWT) analysis[36,37] (SI Figure S3 c-d). In general, CWT analysis has been used to conduct source apportionment of various components such as BC[38], aerosol optical depth[39], atmopsheric mercury[40]. Here we have performed CWT analysis for BC measured at the two receptor sites during SAPOEX-16 (see SI Figure S3 c-d). During CWT analysis, the values of BC concentrations are assigned to the respective BTs and a weighted concentration is allocated to the sequence of grid cells based on the residence time of the BTs as follows :

$$C_{ij} = \frac{\sum_{l=1}^{L} C_l \tau_{\tau_{ijl}}}{\sum_{l=1}^{L} \tau_{\tau_{ijl}}} \qquad (4)$$

where, C_{ij} is the average weighted concentration in ijth grid cell, C_l is the measured BC concentration of a sample, τ_{ijl} is the no. of trajectory endpoints in the ijth grid cell associated with C_l sample, L is the total number of BTs. The CWT analysis confirms quantitatively that the most important potential source regions of BC emissions influencing sampling at MCOH during January was the IGP. A particular observation in the CWT analysis is that the peninsular Indian region was the dominant BC emitting source region during ARS and SE Asia air mass clusters at MCOH (see SI Figures S2-S3). Sampling at BCOB, as inferred from cluster analysis as well, was mainly influenced by BC emitted in the IGP with minor contributions from the N BOB.

The shift in meteorology, and thereby the source regions influencing MCOH, between January to March 2016 is further corroborated by FLEXPART-derived footprint emission sensitivity maps (see SI Figure S11) and potential source contributions (SI Figure S13).

Supplementary Figures

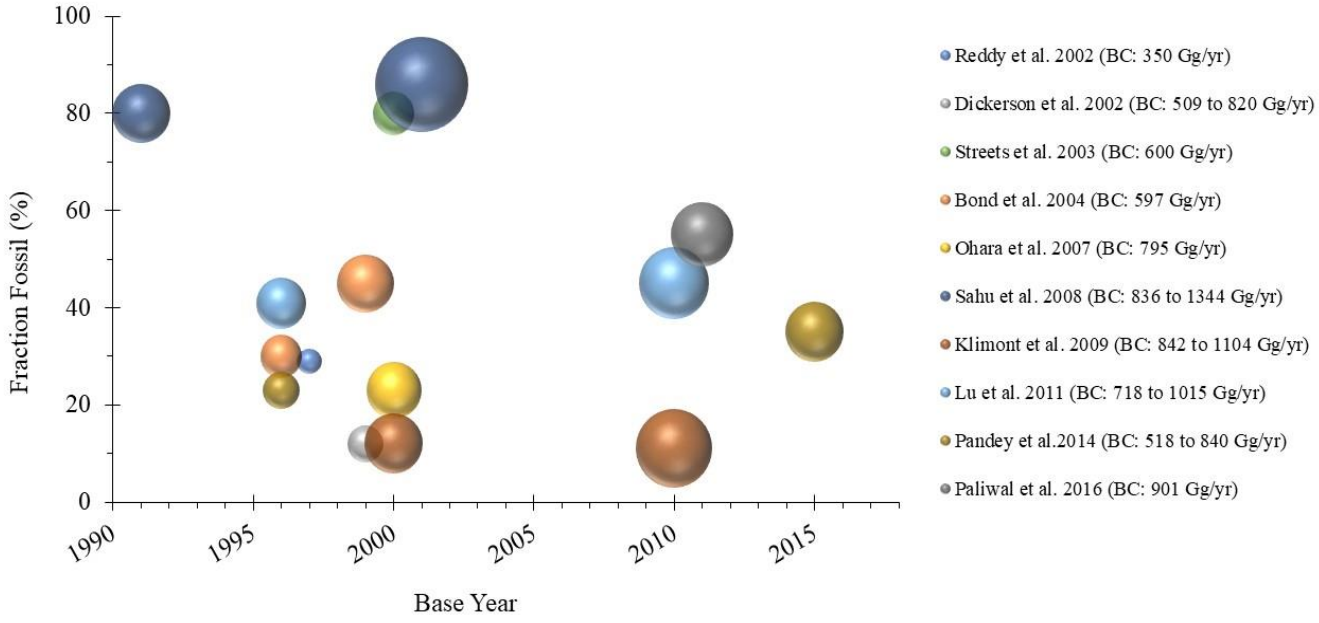

Figure S1. Fraction fossil estimates from bottom-up emission inventories of black carbon (BC) for South Asia as shown in SI Table S1.

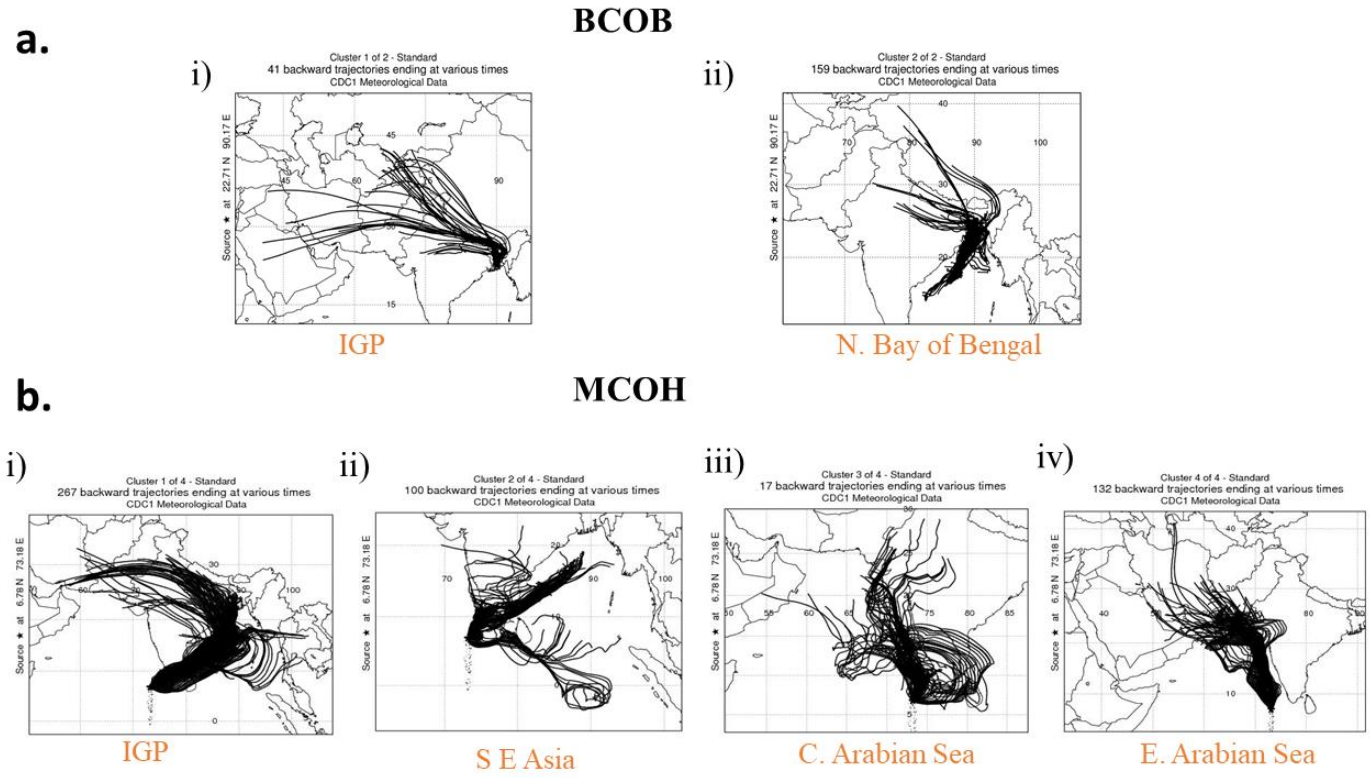

Figure S2. Air mass clusters during the South Asian Pollution Experiment 2016 (SAPOEX-16). See methodological description in SI Note S7.

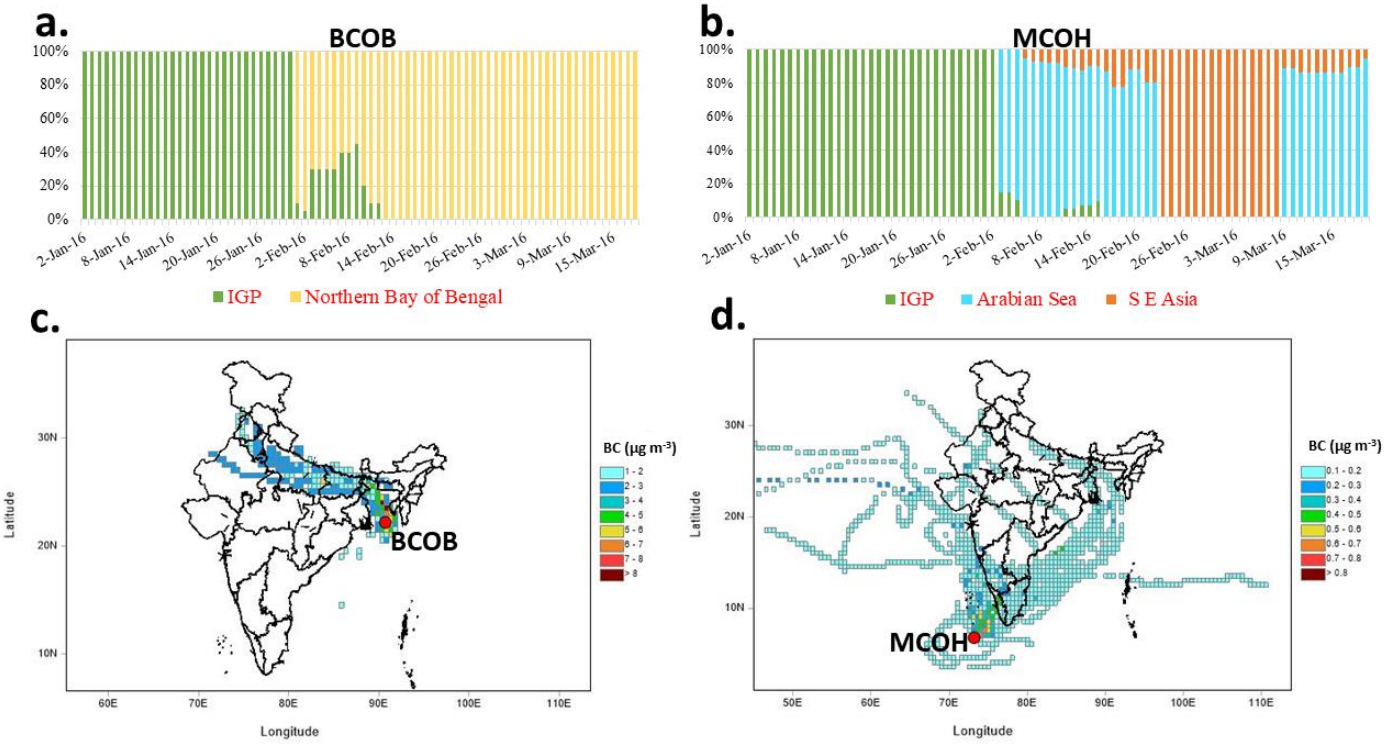

Figure S3. Identification of potential soure regions influencing sampling at receptor sites during SAPOEX-16. (a)(b) The fractional contribution of air mass clusters to the sampling conducted at the Bangladesh Climate Observatory at Bhola (BCOB) and the Maldives Climate Observatory at Hanimaadhoo (MCOH) are shown, respectively. Note the fractional contribution of Central and Eastern Arabian Sea cluster (see SI Figure S2) is here shown as a single air mass cluster (Arabian Sea) at MCOH. **(c)(d)** The Concentration weighted trajectory (CWT) maps for black carbon (BC) mass concentrations (µg m^{-3}) at BCOB and MCOH during SAPOEX-16 are shown, respectively (methodological details in SI Note S7). Color scale represents the BC mass concentrations. Note that IGP during January and peninsular India during latter period(Feb+Mar) are the dominant BC emitting source regions influencing sampling at MCOH, respectively.

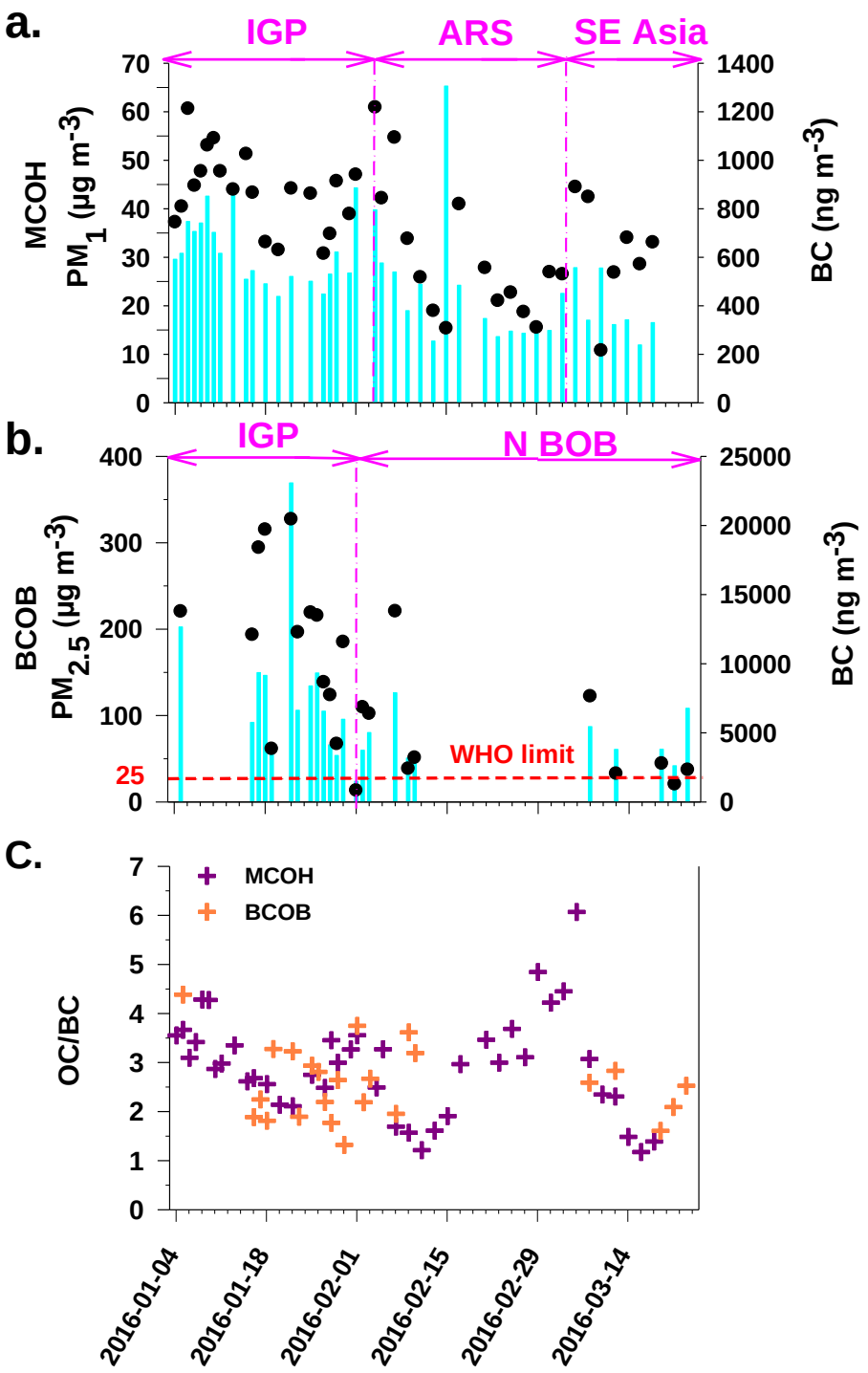

Figure S4. Aerosol characterisitcs during SAPOEX-16. (a) BC (black circles) and PM_1 concentrations (bars; cyan) at the Maldives Climate Observatory at Hanimaadhoo, MCOH; **(b)** BC and $PM_{2.5}$ concentrations at Bangladesh Climate Observatory at Bhola, BCOB; The dotted red line represents the WHO limit for $PM_{2.5}$ loadings as an ambient air quality standard for 24h (25 µg m^{-3}). **(c)** The organic carbon (OC) to black carbon (BC) ratio is shown for both sites. The air mass source regions (IGP, ARS, SE Asia, N BOB) are identified using detailed back trajectory analysis (SI Figure S2-S3; see also SI Note S7).

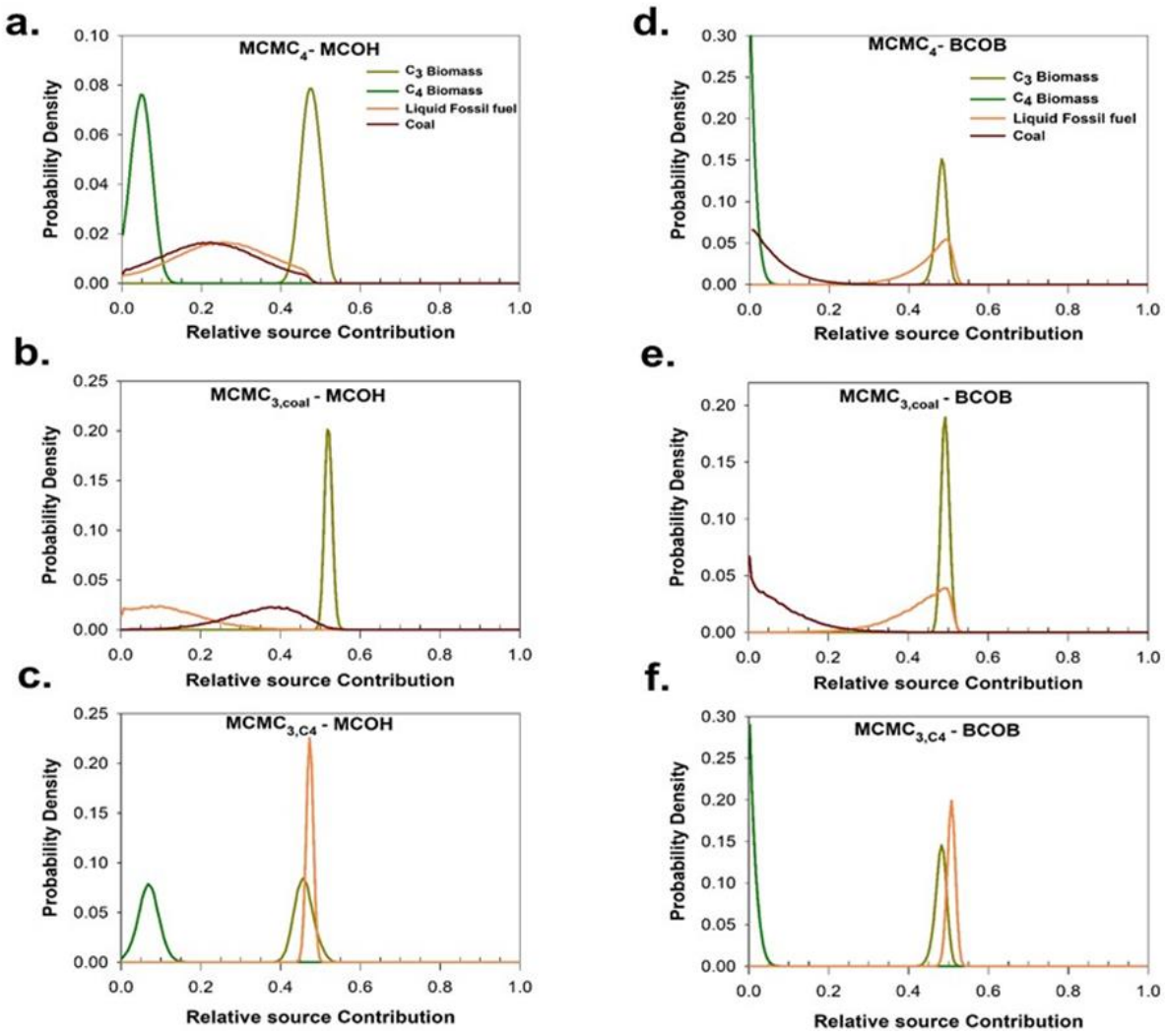

Figure S5. ***Posterior*** **probability density functions (PDFs) of relative source contributions.** For four major sources (C_3 biomass, C_4 biomass, liquid fossil fuel and fossil coal) of black carbon aerosols at MCOH **(a-c)** and BCOB **(d-f)** during SAPOEX-16, is calculated using the Bayesian mass-balance source apportionment approach (equation 1 in the manuscript); for the under-determined system with C_3 biomass, C_4 biomass, liquid fossil, and fossil coal ($MCMC_4$), the determined system with C_3 biomass, liquid fossil, and fossil coal ($MCMC_{3,coal}$), the determined system with C_3 biomass, C_4 biomass, and liquid fossil ($MCMC_{3,C4}$).

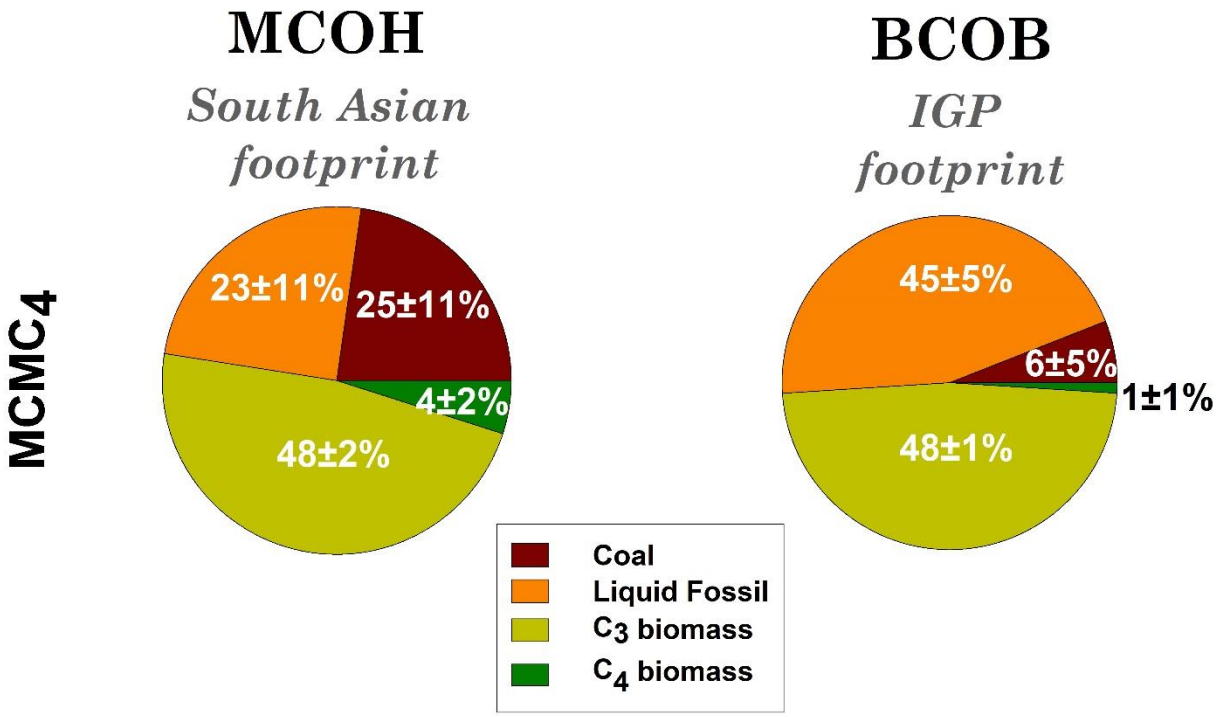

Figure S6. Dual-isotope-constrained source contributions of BC using the MCMC$_4$ scenario. Markov-Chain Monte Carlo (MCMC) based statistical source contributions (Mean ± SD) of fossil coal combustion (brown), liquid fossil fuel combustion (orange) and biomass burning of C_3-plants (light green) and C_4-plants (dark green) to BC at the Maldives Climate Observatory at Hanimaadhoo, MCOH and at Bangladesh Climate Observatory at Bhola, BCOB during SAPOEX-16. Results from a four source (C_3 biomass, C_4 biomass, coal, and liquid fossil) modeling scenario MCMC$_4$ is shown. MCOH is a large-scale oceanic receptor site for South Asia whereas BCOB is a regional receptor site positioned at the outflow of the Indo-Gangetic Plain (IGP), thus each site is representative of a different geographic footprint scale.

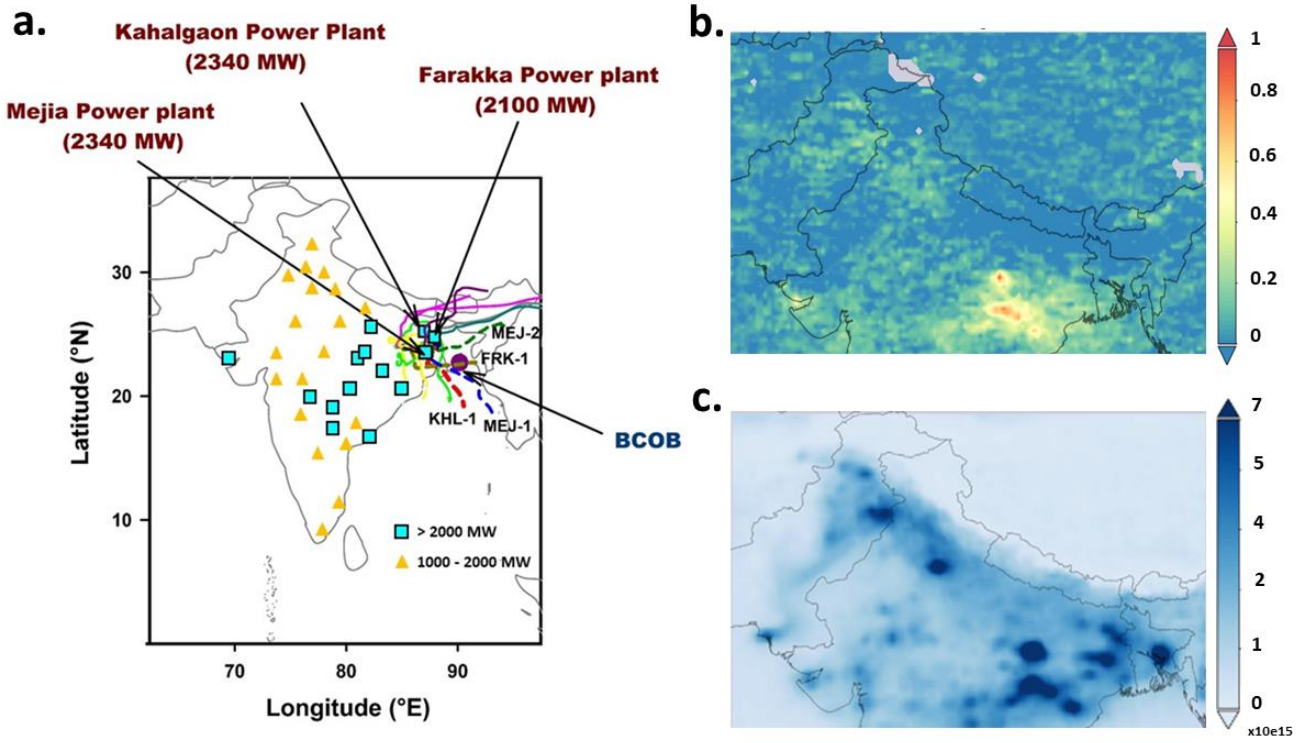

Figure S7. Emissions from coal-fired powerplants in the vicinity of BCOB during SAPOEX-16. **a)** Powerplants with 1000-2000 MW capacity (triangles; yellow), as well as >2000 MW capacity (squares; cyan) and receptor site BCOB are shown. The air mass back-trajectories (in forward mode) from 3 mega powerplants (capacity >2000 MW) - Kahalgaon powerplant (KHL; 25.24°N, 86.98°E), Farakka powerplant (FRK; 25.24°N, 86.98°E), Mejia powerplant (MEJ; 25.24°N, 86.98°E) were generated as in SI Figure S2 for samples used for isotopic investigation of BC (details of samples are provided in SI Table S3). A modest emission height of 300m (stack height 250m + plume rise 50m) was assumed based on data reported in literature[20] and was used as a starting height for the trajectories. Note that of 21 trajectories (representing stack emissions) only 4 trajectories seem to be passing close to/over BCOB, which are shown as dotted lines and referenced to the respective powerplant; namely KHL-1 (dotted ; red), FRK-1 (dotted ; dark yellow), MEJ-1 (dotted ; blue), MEJ-2 (dotted ; dark green). Further investigation of effect of boundary layer can be seen in SI Figure S8. Time-averaged map of **(b)** SO_2 column amount (DU, 1 DU = 2.69 × 10^{16} molecules cm^{-2} **(c)** NO_2 tropospheric column density (molecules cm−2), for the IGP region during SAPOEX-16 (Jan-Mar 2016) are also shown. The SO_2 and NO_2 data were obtained from the OMI instrument on board the Aura satellite (https://giovanni.gsfc.nasa.gov/giovanni/).

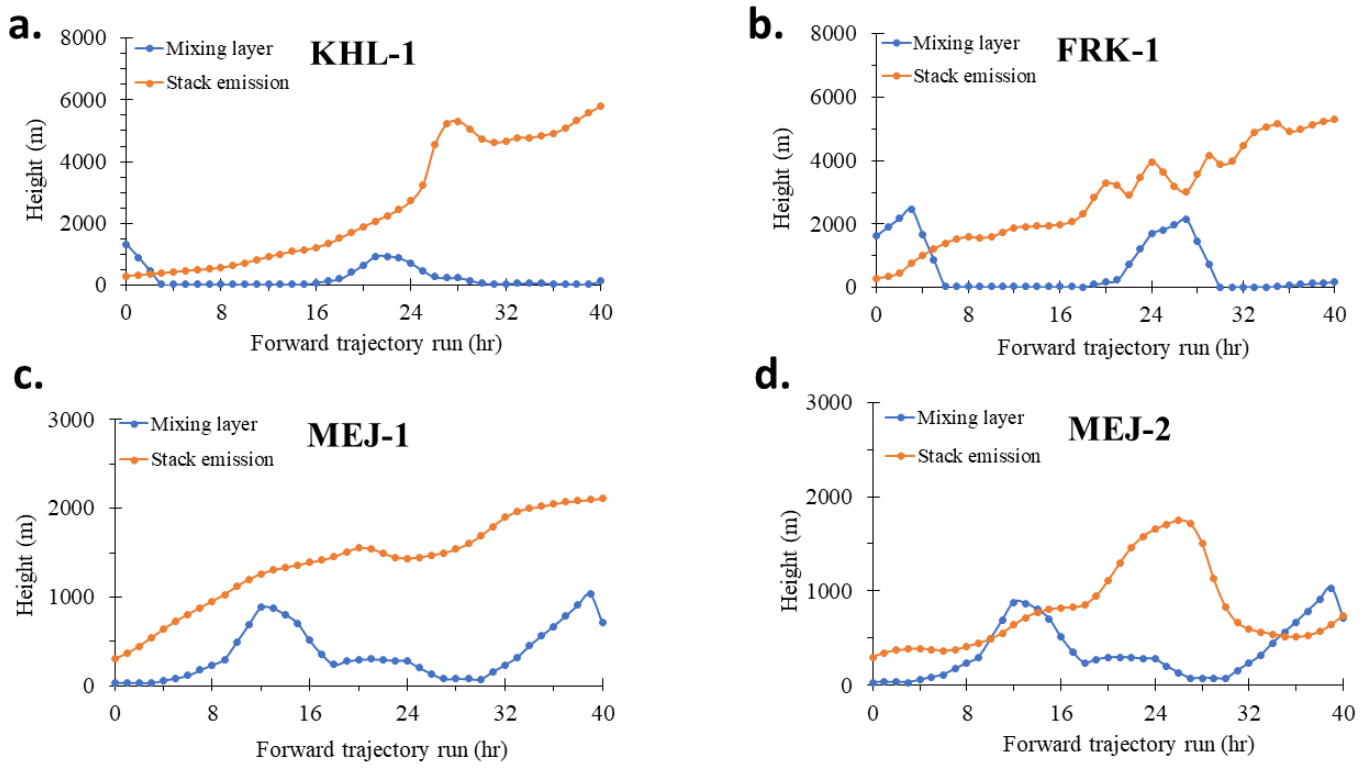

Figure S8. Coupled investigation of mixing layer and powerplant stack emissions. The height of four air mass trajectories (dotted lines in SI Figure S7) represeting stack emissions from three mega coal-fired powerplants [Khalagaon (KHL), Farakka (FRK), Mejia (MEJ)] during transport to BCOB are shown along with the height of the mxing layer. Note the stack emisisons were found to pass-by BCOB within 24h, however, a longer forward run of 40h is shown here to elucidate any possible effects of the mixing layer. It should be noted that particles shot higher up from satcks of relatively lower height than considered here might also end up outside the mixing layer, thereby not making it to ground-level sampling at BCOB.

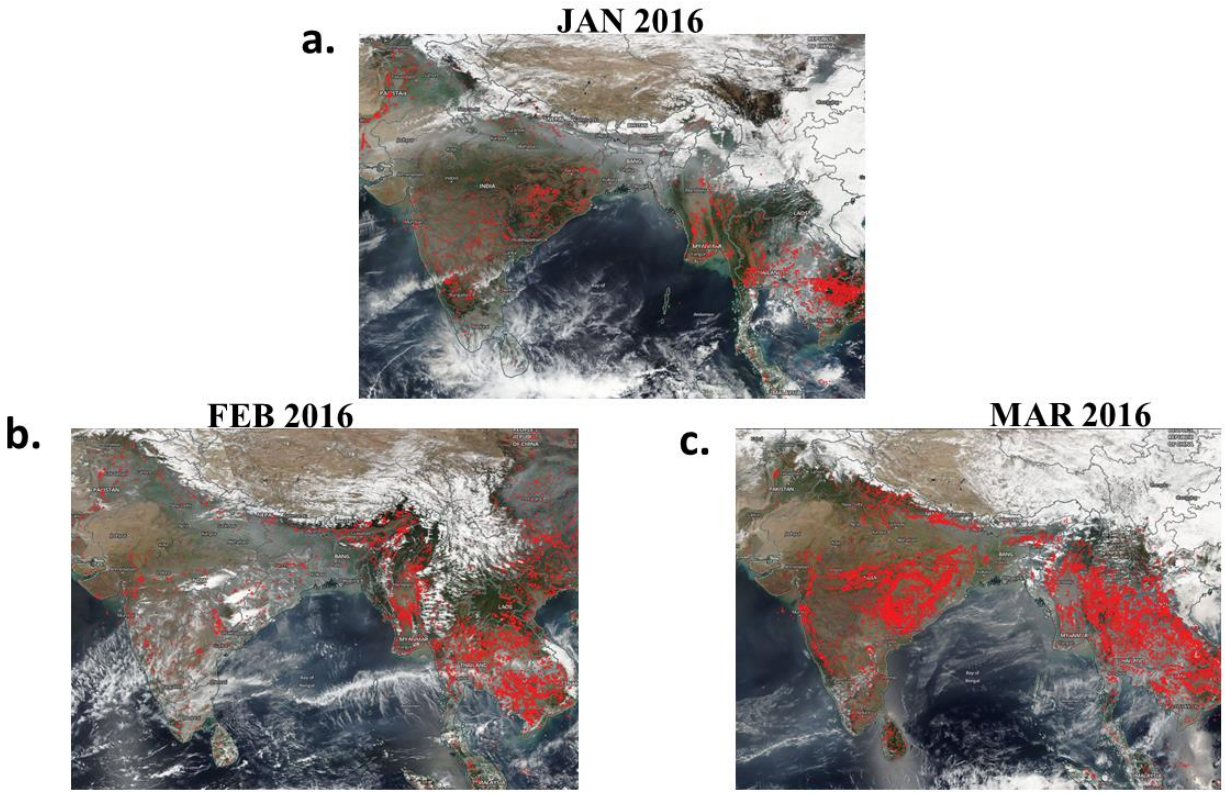

Figure S9. Satellite-derived active fire counts during SAPOEX-16. Active Fire counts are shown for (a) January, (b) February, (c) March 2016, respectively. The fire count data is downloaded from the Fire Information for Resource Management System (NASA-FIRMS) website (last visited 10 March 2020) : https://firms2.modaps.eosdis.nasa.gov/. Note satellite detection of fires is prone to cloud cover and weak thermal signatures of small-scale fires[19].

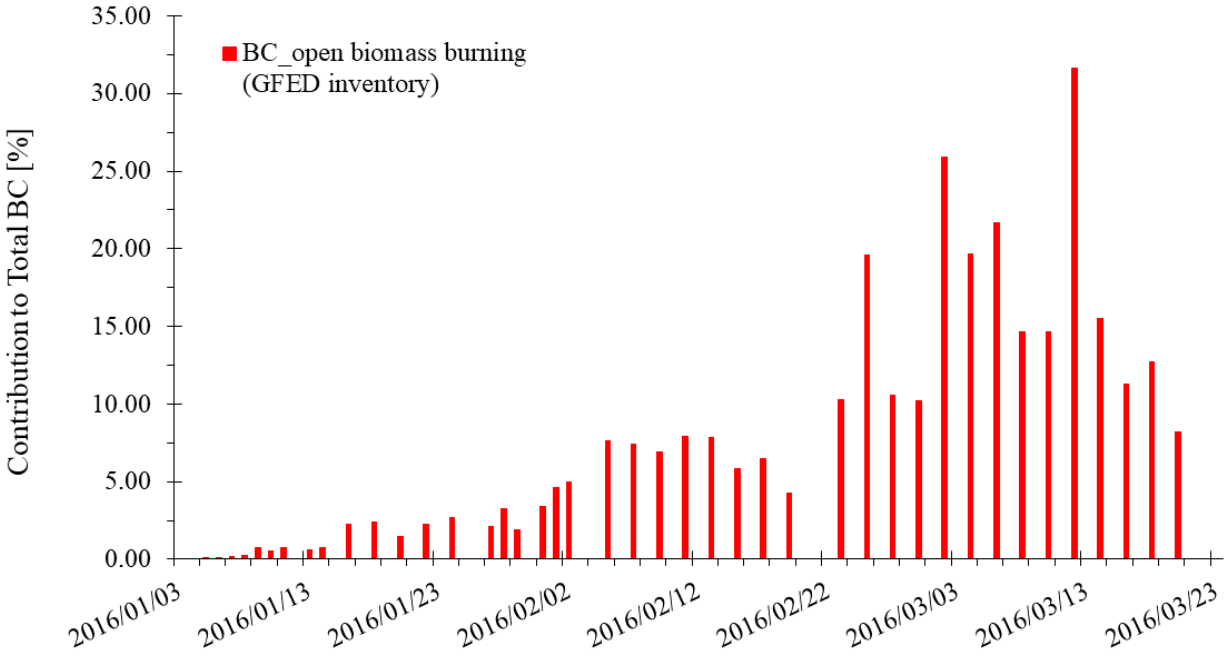

Figure S10. GFED inventory-based BC emissions. Agricultural waste burning (on fields) i.e., open biomass burning contribution to total BC is estimated by the FLEXPART-ECLIPSE-GFED simulations. Note the increase in contribution of BC from open biomass burning from Jan-to-Feb-to-Mar 2016. See SI Table S6 for BC-Fire data. This is also corroborated by a slight trend in $\Delta^{14}C$-f_{bio} between different air mass influenced periods at MCOH (f_{bio}-Jan: 49±4%; f_{bio}-Mar: 58±5%; see SI Table S4), which together suggest that open burning activities occurred in the latter half of the winter period in peninsular India (see also SI Figures S9, S11 and S13) affecting the sampling at MCOH.

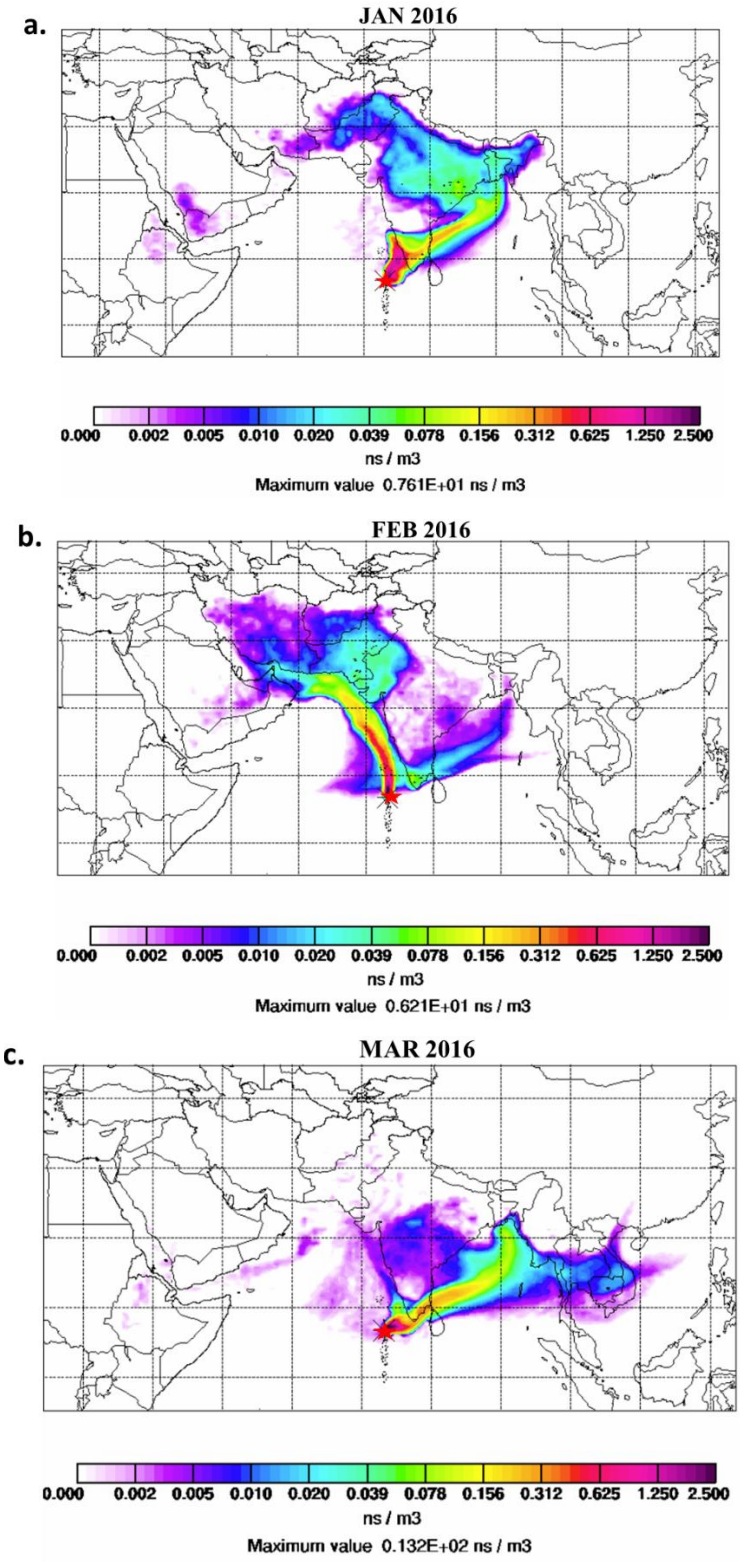

Figure S11. Chemical transport model—FLEXPART—based footprint emission sensitivity (FES). FES maps for the black carbon aerosol tracer arriving at Maldives Climate Observatory at Hanimaadhoo (MCOH) (red star) characteristic of (a) January, (b) February, (c) March of 2016 are shown. Note the HYSPLIT cluster analysis based fractional contribution of air mass clusters (SI Figure S3) compared well with the FLEXPART-based FES.

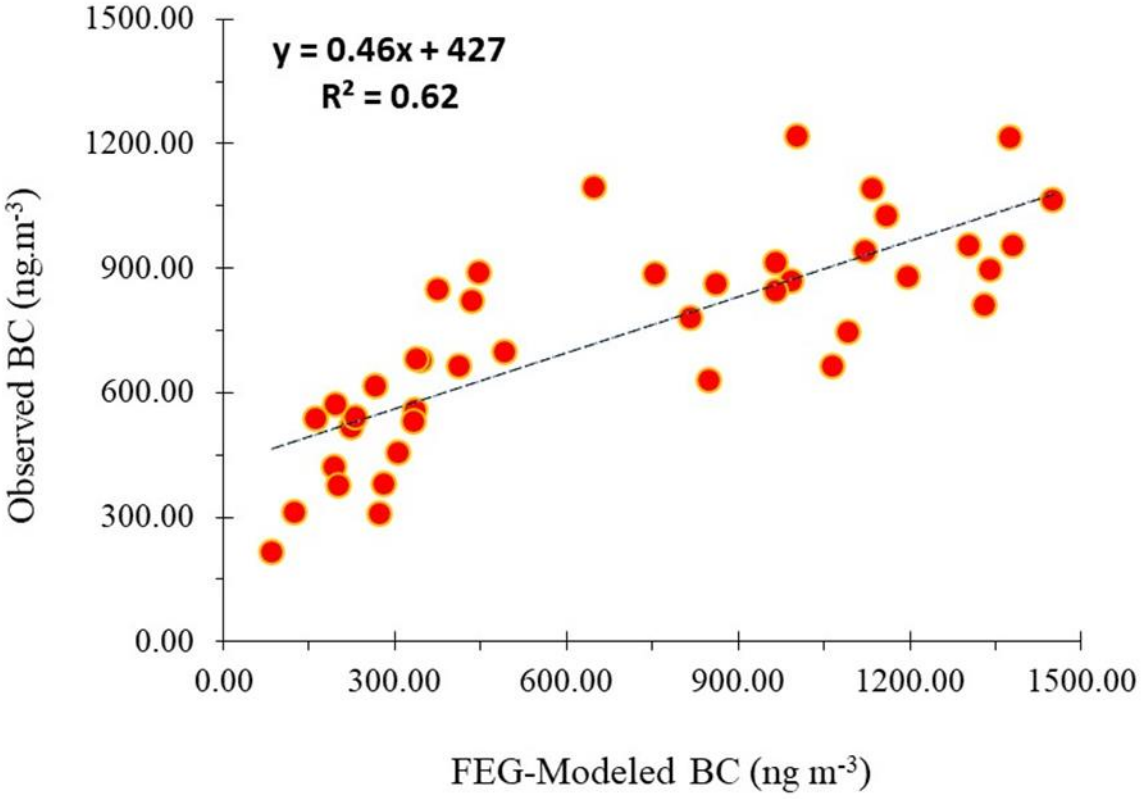

Figure S12. Observed vs. FLEXPART-ECLIPSE-GFED (FEG)-modeled BC concentrations at MCOH.

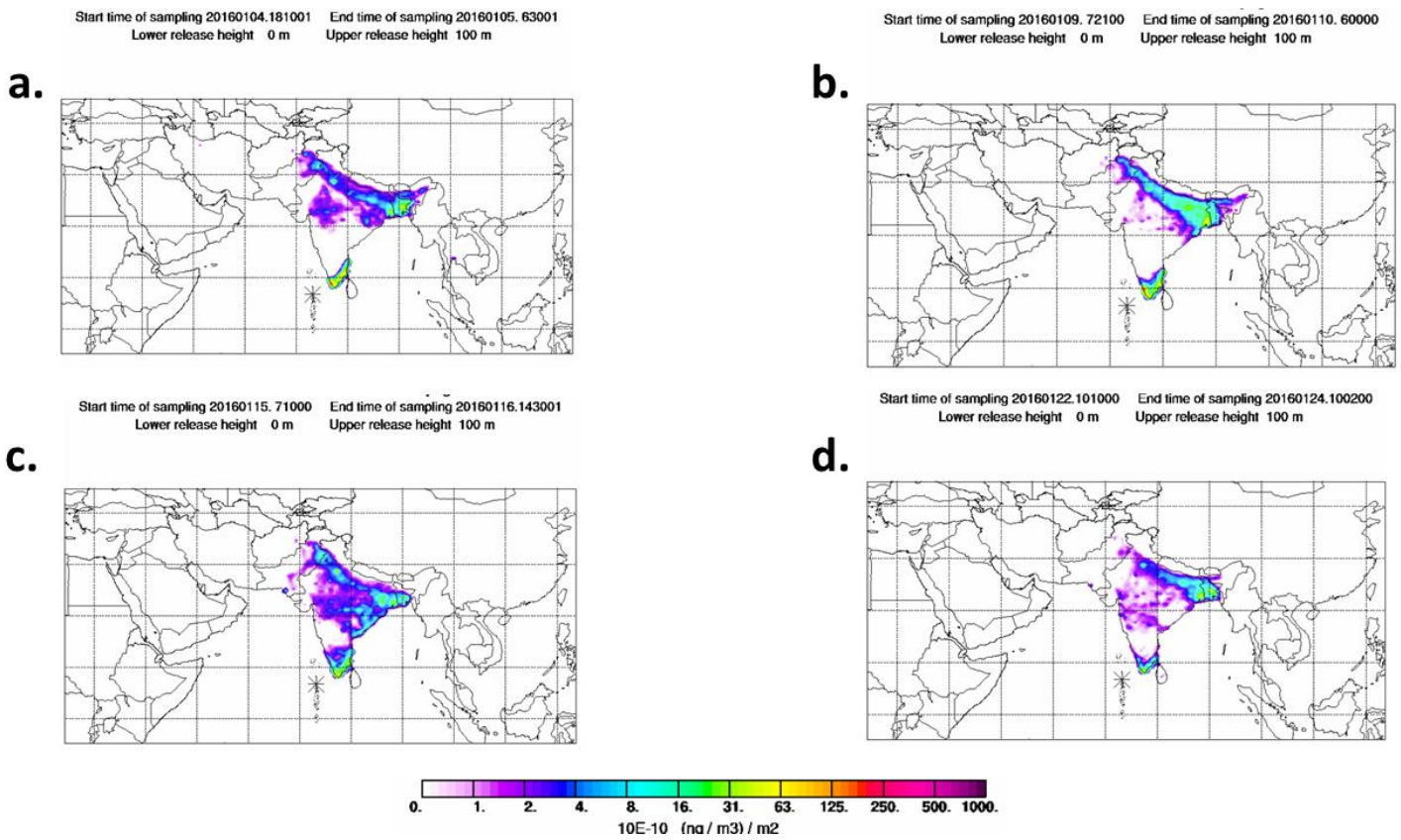
a.
Start time of sampling 20160104.181001 End time of sampling 20160105. 63001
Lower release height 0 m Upper release height 100 m
b.
Start time of sampling 20160109. 72100 End time of sampling 20160110. 60000
Lower release height 0 m Upper release height 100 m
c.
Start time of sampling 20160115. 71000 End time of sampling 20160116.143001
Lower release height 0 m Upper release height 100 m
d.
Start time of sampling 20160122.101000 End time of sampling 20160124.100200
Lower release height 0 m Upper release height 100 m
0. 1. 2. 4. 8. 16. 31. 63. 125. 250. 500. 1000.
10E-10 (ng / m3) / m2

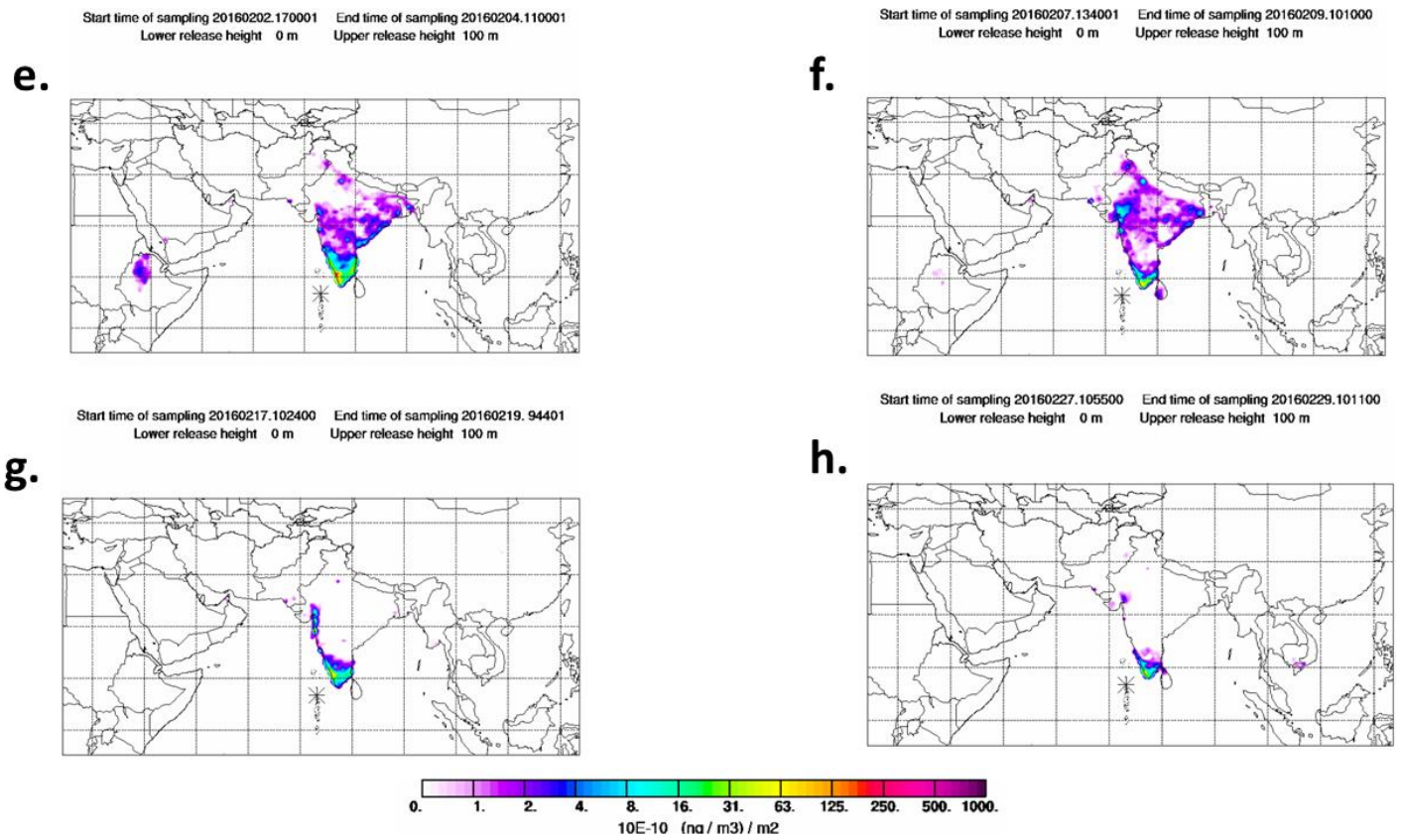
e.
Start time of sampling 20160202.170001 End time of sampling 20160204.110001
Lower release height 0 m Upper release height 100 m
f.
Start time of sampling 20160207.134001 End time of sampling 20160209.101000
Lower release height 0 m Upper release height 100 m
g.
Start time of sampling 20160217.102400 End time of sampling 20160219. 94401
Lower release height 0 m Upper release height 100 m
h.
Start time of sampling 20160227.105500 End time of sampling 20160229.101100
Lower release height 0 m Upper release height 100 m
0. 1. 2. 4. 8. 16. 31. 63. 125. 250. 500. 1000.
10E-10 (ng / m3) / m2

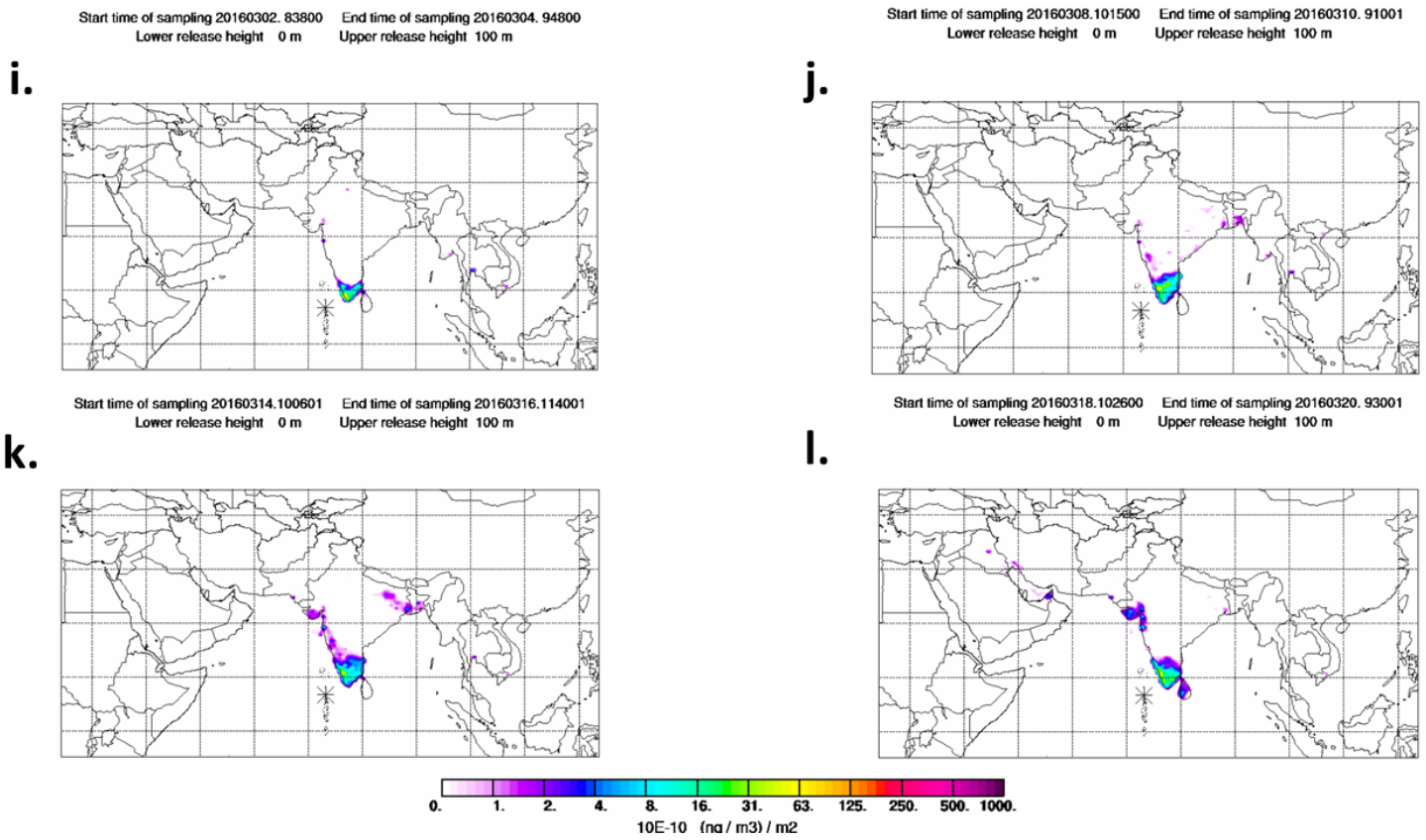

Figure S13. FLEXPART-ECLIPSE-GFED-based anthropogenic black carbon (BC) source contribution to the simulated mixing ratios at MCOH during SAPOEX-16. Shown for early, mid and late periods in January 2016: (**a**) 2016-01-04 to 2016-01-05, (**b**) 2016-01-09 to 2016-01-10, (**c**) 2016-01-15 to 2016-01-16, (**d**) 2016-01-22 to 2016-01-24; February 2016: (**e**) 2016-02-02 to 2016-02-04, (**f**) 2016-02-07 to 2016-02-09, (**g**) 2016-02-17 to 2016-02-19, (**h**) 2016-02-27 to 2016-02-29; and in March 2016: (**i**) 2016-03-02 to 2016-03-04, (**j**) 2016-03-08 to 2016-03-10, (**k**) 2016-03-14 to 2016-03-16, (**l**) 2016-03-18 to 2016-03-20. Note the shift in dominant sources regions – IGP in Jan to Peninsular India (~ south of 23.4°N) in February and March 2016 (see also SI Figure S3 and S11).

Supplementary Tables

Table S1. Fraction fossil estimates from bottom-up emission inventories of BC for South Asia. The compilation is based on previous publications[9,21-30]; asterisk refers to emission inventory predictions for a future base year. A plot of the same can be seen in SI Figure S1.

Emission Inventory	Base Year	Total BC (Gg/yr)	Fraction Fossil (%)
Reddy et al., 2002	1997	350	29
Dickerson et al., 2002	1999	509	12
Streets et al., 2003	2000	600	80
Bond et al., 2004	1996	597	30
Bond et al., 2004*	1999	820	45
Ohara et al., 2007	2000	795	23
Sahu et al., 2008	1991	836	80
Sahu et al., 2008*	2001	1344	86
Klimont et al., 2009	2000	842	12
Klimont et al., 2009*	2010	1104	11
Lu et al., 2011	1996	718	41
Lu et al., 2011	2010	1015	45
Pandey et al., 2014	1996	518	23
Pandey et al., 2014	2015	840	35
Paliwal et al., 2016	2011	901	55

Table S2. Sampling details at MCOH during SAPOEX-16. The sampling details and PM_1, organic carbon (OC) and elemental carbon [EC; referred to as black carbon (BC) in the manuscript] concentrations are shown. Note EC is shown in ng m^{-3}. The sample ID's not mentioned here are samples collected as blanks.

Sample ID	Start date (yr-mo-day)	Start time (hh:min)	Stop date (yr-mo-day)	Stop time (hh:min)	PM_1 ($\mu g/m^3$)	OC ($\mu g/m^3$)	EC (ng/m^3)
1	2016-01-04	18:10	2016-01-05	06:30	30	3	745
2	2016-01-05	09:38	2016-01-06	06:00	31	3	809
3	2016-01-06	09:54	2016-01-07	06:00	37	4	1213
4	2016-01-07	06:00	2016-01-08	06:00	35	3	895
5	2016-01-08	06:00	2016-01-09	06:00	37	4	954
6	2016-01-09	07:21	2016-01-10	06:00	43	4	1062
7	2016-01-10	09:40	2016-01-11	06:00	35	3	1091
8	2016-01-11	08:05	2016-01-13	17:50	31	3	954
9	2016-01-13	19:00	2016-01-14	16:30	45	3	879
10	2016-01-15	07:10	2016-01-16	14:30	25	3	1026
12	2016-01-16	16:57	2016-01-18	10:45	27	2	866
13	2016-01-18	11:09	2016-01-20	10:01	24	2	663
15	2016-01-20	11:10	2016-01-22	09:36	22	1	630
16	2016-01-22	10:10	2016-01-24	10:02	26	2	884
18	2016-01-25	09:40	2016-01-27	09:15	25	2	863
20	2016-01-27	10:00	2016-01-28	13:41	22	2	615
21	2016-01-28	14:20	2016-01-29	17:42	26	2	697
22	2016-01-29	18:25	2016-01-31	10:17	31	3	914
23	2016-01-31	10:55	2016-02-01	10:08	27	2	779
24	2016-02-01	17:58	2016-02-02	10:10	44	3	940
26	2016-02-04	11:15	2016-02-05	11:40	40	3	1218
27	2016-02-05	16:11	2016-02-07	13:33	29	3	844

28	2016-02-07	13:40	2016-02-09	10:10	27	2	1094
30	2016-02-09	11:10	2016-02-11	11:30	19	1	676
31	2016-02-11	12:40	2016-02-13	11:39	24	1	517
32	2016-02-13	12:40	2016-02-15	09:30	13	1	379
34	2016-02-15	10:31	2016-02-17	10:00	65	1	307
35	2016-02-17	10:24	2016-02-19	09:44	24	2	819
37	2016-02-21	10:32	2016-02-23	10:00	17	2	557
38	2016-02-23	10:30	2016-02-25	10:00	14	2	421
39	2016-02-25	10:15	2016-02-27	10:25	15	1	454
40	2016-02-27	10:55	2016-02-29	10:11	14	2	374
42	2016-02-29	11:00	2016-03-02	08:38	16	3	311
43	2016-03-02	08:38	2016-03-04	09:48	15	2	538
44	2016-03-04	09:48	2016-03-06	10:00	23	3	530
45	2016-03-06	10:45	2016-03-08	09:39	28	3	890
46	2016-03-08	10:15	2016-03-10	09:10	17	2	849
47	2016-03-10	09:37	2016-03-12	09:45	28	2	216
48	2016-03-12	09:45	2016-03-14	10:03	16	1	537
50	2016-03-14	10:06	2016-03-16	11:40	17	1	681
51	2016-03-16	12:10	2016-03-18	09:56	12	0	571
52	2016-03-18	10:26	2016-03-20	09:30	17	1	662

Table S3. Sampling details at BCOB during SAPOEX-16. The sampling details and $PM_{2.5}$, organic carbon (OC) and elemental carbon [EC; referred to as black carbon (BC) in the manuscript] concentrations are shown. Note EC is shown in μg m^{-3}. The sample ID's not mentioned here are samples collected as blanks.

Sample ID	Start date (yr-mo-day)	Start time (hh:min)	Stop date (yr-mo-day)	Stop time (hh:min)	$PM_{2.5}$ ($\mu g/m^3$)	OC ($\mu g/m^3$)	EC ($\mu g/m^3$)
114	2016-01-05	15:28	2016-01-06	9:15	203	61	14
116	2016-01-16	18:03	2016-01-17	6:40	92	23	12
117	2016-01-17	16:01	2016-01-18	6:05	150	42	18
118	2016-01-18	17:50	2016-01-19	7:04	146	36	20
119	2016-01-19	16:24	2016-01-20	7:57	59	13	4
120	2016-01-22	16:57	2016-01-23	8:20	369	66	20
121	2016-01-23	17:14	2016-01-24	8:00	106	23	12
123	2016-01-25	17:09	2016-01-26	8:04	134	40	14
124	2016-01-26	16:54	2016-01-27	8:07	149	38	13
125	2016-01-27	16:28	2016-01-28	8:07	105	19	9
126	2016-01-28	17:07	2016-01-29	8:01	66	14	8
127	2016-01-29	17:13	2016-01-30	7:55	54	11	4
128	2016-01-30	17:08	2016-01-31	8:10	96	15	12
129	2016-02-01	17:10	2016-02-02	4:44	24	3	1
130	2016-02-02	17:00	2016-02-03	4:45	60	15	7
131	2016-02-03	17:01	2016-02-04	7:30	80	17	6
132	2016-02-07	9:14	2016-02-08	6:30	126	27	14
133	2016-02-09	7:56	2016-02-10	7:05	51	9	2
134	2016-02-10	16:50	2016-02-11	15:40	57	10	3
142	2016-03-08	16:30	2016-03-09	16:35	87	20	8
144	2016-03-12	17:03	2016-03-13	16:21	61	6	2
147	2016-03-19	16:30	2016-03-20	8:06	61	5	3
148	2016-03-21	10:51	2016-03-22	16:20	42	3	1
149	2016-03-23	16:30	2016-03-24	16:15	109	6	2

Note there were frequent power outages for long duration at BCOB, which was common in Bangladesh in 2016 and more so in remote locations[31], this was a deterrent for continuous 24h sampling.

Table S4. Isotope signatures of ambient BC collected at the BCOB and MCOH during SAPOEX-16. BHL here refers to BCOB. A discussion on SPX-BHL-121 sample is provided in SI Note S4. The isolates of SPX-BHL-114, SPX-MCOH-32 did not contain enough C-amount for $\delta^{13}C$ analysis and hence the data cannot be reported. Fraction biomass burning (f_{bio}) is calculated based on eqn. 1 provided in main manuscript.

Sample ID	Accession #	F Modern (F_m)	F_m Err	$\delta^{13}C_{BC}$ (‰)	$\Delta^{14}C_{BC}$ (‰)	f_{bio} (‰)
SPX-BHL-116	OS-137338	0.51280	0.00300	-27.58	-491	48
SPX-BHL-117	OS-137339	0.52460	0.00300	-27.23	-479	49
SPX-BHL-118	OS-137340	0.56140	0.00270	-27.14	-443	52
SPX-BHL-123	OS-137342	0.53890	0.00260	-27.36	-465	50
SPX-BHL-132	OS-141036	0.58900	0.00170	-26.85	-415	55
SPX-BHL-142	OS-141037	0.54250	0.00140	-27.04	-461	50
SPX-BHL-149	OS-140962	0.47450	0.00200	-27.05	-529	44
SPX-BHL-114	OS-137337	0.58110	0.00280	NA	-423	54
SPX-BHL-121	OS-141179	0.01180	0.00190	-31.49	-988	
SPX-MCOH-5	OS-137344	0.50240	0.00330	-24.93	-501	47
SPX-MCOH-10	OS-137742	0.50000	0.00220	-24.67	-504	46
SPX-MCOH-13	OS-137345	0.58130	0.00270	-24.57	-423	54
SPX-MCOH-16	OS-137346	0.55170	0.00320	-24.92	-452	51
SPX-MCOH-30	OS-137738	0.47570	0.00420	-25.12	-528	44
SPX-MCOH-31	OS-137343	0.60360	0.00270	-25.13	-401	56
SPX-MCOH-45	OS-137740	0.62340	0.00320	-25.29	-381	58
SPX-MCOH-46	OS-137361	0.67580	0.00270	-25	-329	63
SPX-MCOH-47	OS-137741	0.56690	0.00400	-25.42	-437	53
SPX-MCOH-32	OS-137739	0.43260	0.00530	NA	-570	40

Note the slight trend in $\Delta^{14}C$-f_{bio} between different air mass influenced periods at MCOH (f_{bio}-Jan: 49±4%; f_{bio}-Mar: 58±5%; see also SI Table S2, SI Figures S2-S3), while at BCOB, no such trend in $\Delta^{14}C$-f_{bio} is evident for the winter of 2016 (f_{bio}-Jan: 50±2%; f_{bio}-Mar: 50±6%). However, this had no discernible effect on the $\delta^{13}C$ signals at both sites. It is presently unclear as to how the $\delta^{13}C$ isotopic signals are expected to vary with changes in $\Delta^{14}C$ signals in the South Asian BC aerosol context.

Table S5. Radiocarbon ($\Delta^{14}C$) and stable carbon ($\delta^{13}C$) endmember values for different BC sources.

	C_3-biomass	C_4-biomass	Liquid Fossil fuel	Fossil Coal
$\Delta^{14}C$	+77±60	+20±10	-1000	-1000
$\delta^{13}C$	-27.1±2	-13.1±1.2	-25.5±1.3	-23.4±1.3

Note the choice of endmembers for $\Delta^{14}C$ biomass (C_3, C_4) are detailed in SI Notes S1-S3. Since C_4 plants are overall annual plants, the $\Delta^{14}C_{C4\text{-plants}}$ was set to +20±10‰, whereas for $\Delta^{14}C_{C3\text{-plants}}$ the value of +77±60‰ was estimated (See SI Table S8). $\delta^{13}C$ biomass (C_3, C_4) are adopted from elsewhere[10]. Fossil endmembers are unchanged as in a previous publication[11].

Table S6. FLEXPART-ECLIPSE-GFED (FEG) model predictions during SAPOEX-16. Simulations are based on tailored-simulations corresponding to filter-based ambient aerosol sample collection at MCOH. Note the black carbon (BC) emissions from agricultural waste burning (on fields; BC-Fire) i.e., open biomass burning is included using the Global Fire Emissions Database (GFED) inventory.

Sample Set no	Start date (yr-mo-day)	Start time (hh:min)	Stop date (yr-mo-day)	Stop time (hh:min)	BC-Total (ng/m3)	BC-Fire (ng/m^3)	BC-Biofuel (ng/m^3)	BC-Fossil (ng/m^3)
1	2016-01-04	18:10	2016-01-05	06:30	1094	0	400	694
2	2016-01-05	09:38	2016-01-06	06:00	1332	2	498	832
3	2016-01-06	09:54	2016-01-07	06:00	1375	3	515	857
4	2016-01-07	06:00	2016-01-08	06:00	1342	3	498	840
5	2016-01-08	06:00	2016-01-09	06:00	1304	10	482	812
6	2016-01-09	07:21	2016-01-10	06:00	1451	7	545	899
7	2016-01-10	09:40	2016-01-11	06:00	1136	9	421	706
8	2016-01-11	08:05	2016-01-13	17:50	1381	8	510	862
9	2016-01-13	19:00	2016-01-14	16:30	1196	9	444	744
10	2016-01-15	07:10	2016-01-16	14:30	1159	26	448	684
12	2016-01-16	16:57	2016-01-18	10:45	993	24	376	593
13	2016-01-18	11:09	2016-01-20	10:01	1065	16	412	637
15	2016-01-20	11:10	2016-01-22	09:36	850	19	326	505
16	2016-01-22	10:10	2016-01-24	10:02	756	20	287	448
18	2016-01-25	09:40	2016-01-27	09:15	863	18	312	533
20	2016-01-27	10:00	2016-01-28	13:41	266	9	86	171
21	2016-01-28	14:20	2016-01-29	17:42	492	9	180	303
22	2016-01-29	18:25	2016-01-31	10:17	967	33	354	580
23	2016-01-31	10:55	2016-02-01	10:08	817	38	316	463
24	2016-02-01	17:58	2016-02-02	10:10	1122	56	411	655
26	2016-02-04	11:15	2016-02-05	11:40	1003	77	380	546
27	2016-02-05	16:11	2016-02-07	13:33	966	71	368	527
28	2016-02-07	13:40	2016-02-09	10:10	648	45	244	359
30	2016-02-09	11:10	2016-02-11	11:30	347	28	129	190
31	2016-02-11	12:40	2016-02-13	11:39	225	18	84	123
32	2016-02-13	12:40	2016-02-15	09:30	283	17	108	158
34	2016-02-15	10:31	2016-02-17	10:00	274	18	92	165
35	2016-02-17	10:24	2016-02-19	09:44	436	19	148	269
37	2016-02-21	10:32	2016-02-23	10:00	337	35	119	183

38	2016-02-23	10:30	2016-02-25	10:00	198	38	80	77
39	2016-02-25	10:15	2016-02-27	10:25	307	32	110	165
40	2016-02-27	10:55	2016-02-29	10:11	202	21	72	109
42	2016-02-29	11:00	2016-03-02	08:38	125	32	46	47
43	2016-03-02	08:38	2016-03-04	09:48	231	45	83	102
44	2016-03-04	09:48	2016-03-06	10:00	333	72	122	139
45	2016-03-06	10:45	2016-03-08	09:39	448	66	158	224
46	2016-03-08	10:15	2016-03-10	09:10	377	55	133	188
47	2016-03-10	09:37	2016-03-12	09:45	86	27	39	19
48	2016-03-12	09:45	2016-03-14	10:03	162	25	59	78
50	2016-03-14	10:06	2016-03-16	11:40	340	38	116	185
51	2016-03-16	12:10	2016-03-18	09:56	198	25	66	107
52	2016-03-18	10:26	2016-03-20	09:30	413	34	133	246

Table S7. A compilation of OC/BC ratios for various sites in South Asia.

The locations in the in the Indo-Gangetic Plain are marked as IGP.

Place	OC/BC RATIO	Study
MCOH	3.1 ± 1.5	This study [SAPOEX-16]
BCOB (IGP)	2.5 ±0.8	This study [SAPOEX-16]
Kharagpur (IGP)	7.0 ± 2.2	Bikkina et al., 2014
Hisar (IGP)	8.5 ± 2.2	Rengarajan et al., 2007
Kanpur (IGP)	8.7 ± 3.9	Ram et al., 2010
Patiala (IGP)	11 ± 2	Rajput et al., 2014
Patiala (IGP)	3.0 ± 0.4	Rajput et al., 2014
Dhaka (IGP)	2.1	Salam et al., 2003
Delhi (IGP)	5.0	Tiwari et al., 2013
Agra (IGP)	7.1	Pachauri et al., 2013
Manora Peak (IGP)	6.3 ± 2.2	Ram et al., 2008
Mumbai	2.5	Venkataraman et al., 2002
Adityapur	5.3 ± 1.1	Shubankar et al., 2016
Mt. Abu	4.5 ± 0.9	Ram et al., 2010a
Ahmedabad	6.2	Rengarajan et al., 2011
Srinagar	4.2	Sandeep et al., 2020
Pune	1.16	Ali et al., 2016
Hyderabad	1.39	Ali et al., 2016

Table S8. Computation of the weighted South Asia-specific biomass endmember. Calculations are based on weighed emissions of C_3- and C_4 biomass in various sectors of black carbon biomass emissions. The activity and emission factors (EF) are taken from an up-to-date emission inventory[9]. The contribution of C_3- and C_4 biomass in individual sectors is detailed in SI Note S2, contemporary and aged biomass $\Delta^{14}C$-CO_2 signatures are detailed in SI Note S1.

Sectors	Activity	EF	Emission	Fraction Biomass	Biomass Emission	Fraction C_3	C_3 Emission	Fraction of C_3	Fraction C_3 $\Delta^{14}C$-CO_2	$\Delta^{14}C$-CO_2 (‰)	$\Delta^{14}C$-wood (‰)	$\Delta^{14}C$-of fuel	weighted $\Delta^{14}C_{biomass}$ (‰)
OPEN BURNING													
1. crop residue	94	0.69	65	1	65	0.5	32	0.10	1	20	110	20	2
2. Forest fire	48	0.76	36	1	36	1	36	0.11	0	20	110	110	12
3. Garbage	3	0.51	2	0.5	1	1	1	0.00	0.5	20	110	65	0
DOMESTIC													
4. Dung cake	110	0.47	52	1	52	1	52	0.15	1	20	110	20	3
5. Agri. Residue	103	0.74	76	1	76	0.5	38	0.11	1	20	110	20	2
6. Firewood	229	0.78	178	1	178	1	178	0.53	0	20	110	110	58

Table S9. Emission sector-based partitioning of the bottom-up emission inventory – Evaluating the Climate and Air Quality Impacts of Short-Lived Pollutants (ECLIPSE) data.

Biofuel	Fossil fuel	Fire (GFED)
Residential and commercial	Residential and commercial	Agricultural waste burning
Industry (combustion and processing)	Residential and commercial; non-fuel activity	
Power plants	Power plants, energy conversion, extraction	
	Industry (combustion and processing)	
	Industry (combustion and processing); non-fuel activity	
	Power plants	
	Power plants; non-fuel activity	
	Surface transportation	
	Waste	

Note all available emissions were split according to their source type[15]. Agricultural waste burning (on fields) is included in the Global Fire Emissions Database (GFED). This emission type was hence excluded from the used ECLIPSE emissions.

References

1. Levin, I.; Kromer, B.; Hammer, S. Atmospheric $\Delta^{14}CO_2$ trend in Western European background air from 2000 to 2012. *Tellus B* **2013**, *65*, 20092.

2. Graven, H. D. Impact of fossil fuel emissions on atmospheric radiocarbon and various applications of radiocarbon over this century. *Proc. Natl. Acad. Sci. U. S. A.* **2015**, *112*, 9542–9545.

3. Turnbull1, J. C.; Fletcher, S. E. M.; Ansell, I.; Brailsford, G. W.; Moss, R. C.; Norris, M. W.; Steinkamp, K. Sixty years of radiocarbon dioxide measurements at Wellington, New Zealand: 1954–2014. *Atmos. Chem. Phys.* **2017**, *17*, 14771-14784.

4. Vieira, S.; Trumbose, S.; Camargo, P. B.; Selhorst, D.; Chambers, J. Q.; Higuchi, N.; Martinelli, L. A. Slow growth rates of Amazonian trees: consequences for carbon cycling. *Proc. Natl. Acad. Sci. U. S. A.* **2005**, *102*, 502–507.

5. Mohn, J.; Szidat, S.; Fellner, J.; Rechberger, H.; Quartier, R.; Buchmann, B.; Emmenegger, L. Determination of biogenic and fossil CO_2 emitted by waste incineration based on 14 CO_2 and mass balances. *Biores. Technol.* **2008**, *99*, 6471–6479.

6. Vlam, M.; van der Sleen, P.; Groenendijk, P.; Zuidema, P. A. Tree age distributions reveal large-scale disturbance-recovery cycles in three tropical forests. *Frontiers in Plant Science* **2016**, *7*, 1984.

7. Yoon, S.; Fairley, D.; Barrett, T.; Sheesley, R. Biomass and fossil fuel combustion contributions to elemental carbon across the San Francisco Bay Area. *Atmos. Environ.* **2018**, *195*, 229-242.

8. Zotter, P.; El-Haddad, I.; Zhang, Y.; Hayes, P. L.; Zhang, X.; Lin, Y. H.; Wacker, L.; Schnelle-Kreis, J.; Abbaszade, G.; Zimmermann, R.; Surratt, J. D.; Weber, R.; Jimenez, J. L.; Szidat, S.; Baltensperger, U.; Prévôt, A. S. H. Diurnal cycle of fossil and non-fossil carbon using radiocarbon analyses during CalNex. *J. Geophys. Res. Atmos.* **2014**, *119*, 6818–6835.

9. Paliwal, U.; Sharma, M.; Burkhart, J. F. Monthly and spatially resolved black carbon emission inventory of India: uncertainty analysis. *Atmos. Chem. Phys.* **2016**, *16*, 12457-12476.

10. O'Leary, M. H. Carbon isotopes in photosynthesis. *Bioscience.* **1988**, *38*, 328–336.

11. Andersson, A.; Deng, J.; Ke, D.; Zheng, M.; Yan, C.; Sköld, M.; Gustafsson, Ö. Regionally-varying combustion sources of the January 2013 severe haze events over eastern China. *Environ. Sci. Technol.* **2015**, *49*, 2038–4496.

12. Das, O.; Wang, Y.; Hsieh, Y. P. Chemical and carbon isotopic characteristics of ash and smoke derived from burning of C3 and C4 grasses. *Org. Geochem.* **2010**, *41*, 263–269.

13. Bird, M. I.; Ascough, P. L. Isotopes in pyrogenic carbon: a review. *Org. Geochem.* **2012**, *42*, 1529–1539.

14. Jain, N.; Bhatia, A.; Pathak, H. Emission of air pollutants from crop residue burning in India. *Aerosol Air Qual. Res.* **2014**, *14*, 422–430.

15. Winiger, P.; Andersson, A.; Eckhardt, S.; Stohl, A.; Gustafsson, Ö. The sources of atmospheric black carbon at a European gateway to the Arctic. *Nat. Comm.* **2016**, *7*, 12776.

16. Stohl, A.; Aamaas, B.; Amann, M.; Baker, L. H.; Bellouin, N.; Berntsen, T. K.; Boucher, O.; Cherian, R.; Collins, W.; Daskalakis, N.; Dusinska, M.; Eckhardt, S.; Fuglestvedt, J. S.; Harju, M.; Heyes, C.; Hodnebrog, Ø.; Hao, J.; Im, U.; Kanakidou, M.; Klimont, Z.; Kupiainen, K.; Law, K. S.; Lund, M. T.; Maas, R.; MacIntosh, C. R.; Myhre, G.; Myriokefalitakis, S.; Olivié, D.; Quaas, J.; Quennehen, B.; Raut, J. C.; Rumbold, S. T.; Samset, B. H.; Schulz, M.; Seland, Ø.; Shine, K. P.; Skeie, R. B .; Wang, S.; Yttri, K. E.; Zhu, T. Evaluating the climate and air quality impacts of short-lived pollutants. *Atmos. Chem. Phys*. **2015**, *15*, 10529-10566.

17. Andersson, A. A systematic examination of a random sampling strategy for source apportionment calculations. *Sci. Tot. Environ.* **2011**, *412*, 232–238.

18. Sheesley, R. J.; Andersson, A.; Gustafsson, Ö. Source characterization of organic aerosols using Monte Carlo source apportionment of PAHs at two South Asian receptor sites. *Atmos. Environ.* **2011**, *45*, 3874-3881.

19. Parnell, A.C.; Inger, R.; Bearhop, S.; Jackson, A. L. Source apportionment using stable isotopes: coping with too much variation. *PLOS one* **2010**, *5*, 1-5.

20. Fang, W.; Du, K.; Andersson, A.; Xing, Z.; Cho, C.; Kim, S. W.; Deng, J.; Gustafsson, Ö. Dual-isotope constraints on seasonally resolved source fingerprinting of black carbon aerosols in sites of the four emission hot spot regions of China. *J. Geophy. Res. Atmos*. **2018**, *123*, 11,735–11,747.

21. Li, C.; Bosch, C.; Kang, S.; Andersson, A.; Chen, P.; Zhang, Q.; Cong, Z.; Chen, B.; Qin, D.; Gustafsson, Ö. Sources of black carbon to the Himalayan–Tibetan Plateau glaciers. *Nat. Comm.* **2016**, *7*, 12574.

22. Winiger, P.; Barrett, T. E.; Sheesley, R. J.; Huang, L.; Sharma, S.; Barrie, L. A.; Yttri, K. E.; Evangeliou, N.; Eckhardt, S.; Stohl, A.; Klimont, Z.; Heyes, C.; Semiletov, I. P.; Dudarev, O. V.; Charkin, A.; Shakhova, N.; Holmstrand, H.; Andersson, A.; Gustafsson, Ö. Source apportionment of circum-Arctic atmospheric black carbon from isotopes and modelling. *Sci. Adv.***2019**, *5*, eaau8052.

23. Stohl, A.; Forster, C.; Frank, A.; Seibert, P.; Wotawa, G. Technical note: the Lagrangian particle dispersion model FLEXPART version 6.2. *Atmos. Chem. Phys.* **2005**, *5*, 2461–2474.

24. Stohl, A.; Hittenberger, M.; Wotawa, G. Validation of the lagrangian particle dispersion model FLEXPART against large-scale tracer experiment data. *Atmos. Environ.* **1998**, *32*, 4245–4264.

25. Seibert, P.; Frank, A. Source-receptor matrix calculation with a Lagrangian particle dispersion model in backward mode. *Atmos. Chem. Phys.* **2004**, *4*, 51–63.

26. Stohl, A.; Klimont, Z.; Eckhardt, S.; Kupiainen, K.; Shevchenko, V. P.; Kopeikin, V. M.; Novigatsky, A. N. Black carbon in the Arctic: the underestimated role of gas flaring and residential combustion emissions. *Atmos. Chem. Phys*. **2013**, *13*, 8833–8855.

27. Hertel, O.; Christensen, J.; Runge, E. H.; Asman, W. A. H.; Berkowicz, R.; Hovmand, M. F.; Hov, O. Development and testing of a new variable scale air pollution model – ACDEP. *Atmos. Environ.* **1995**, *29*, 1267–1290.

28. Amann, M.; Bertok, I.; Borken-Kleefeld, J.; Cofala, J.; Heyes, C.; Höglund-Isaksson, L.; Klimont, Z.; Nguyen, B.; Posch, M.; Rafaj, P.; Sandler, R.; Schöpp, W.; Wagner, F.; Winiwarter, W. Cost-effective control of air quality and greenhouse gases in Europe: Modeling and policy applications. *Environ. Modell. Softw.* **2011**, *26*, 1489–1501.

29. Klimont, Z.; Hoglund, L.; Heyes, C.; Rafaj, P.; Schoepp, W.; Cofala, J.; Borken-Kleefeld, J.; Purohit, P.; Kupiainen, K.; Winiwarter, W.; Amann, M.; Zhao, B.; Wang, S. X.; Bertok, I.; Sander, R. Global scenarios of air pollutants and methane: 1990–2050, *In preparation*. https://iiasa.ac.at/web/home/ research/research Programs/air/Global_emissions.html

30. Klimont, Z.; Kupiainen, K.; Heyes, C.; Purohit, P.; Cofala, J.; Rafaj, P.; Borken-Kleefeld, J.; Schoepp, W. Global anthropogenic emissions of particulate matter including black carbon. *Atmos. Chem. Phy.* **2017**, *17*, 8681 - 8723.

31. van der Werf, G. R.; Randerson, J. T.; Giglio, L.; van Leeuwen, T. T.; Chen, Y.; Rogers, B. M.; Mu, M.; van Marle, M. J. E.; Morton, D. C.; Collatz, G. J.; Yokelson, R. J.; Kasibhatla, P. S. Global fire emissions estimates during 1997–2016. *Earth Syst. Sci. Data* **2017**, *9*, 697–720.

32. van der Werf, G. R.; Randerson, J. T.; Giglio, L.; Collatz, G. J.; Mu, M.; Kasibhatla, P. S.; Morton, D. C.; DeFries, R. S.; Jin, Y.; van Leeuwen, T. T. Global fire emissions and the contribution of deforestation, savanna, forest, agricultural, and peat fires (1997–2009). *Atmos. Chem. Phys.* **2010**, *10*, 11707–11735.

33. Giglio, L.; Randerson, J. T.; van der Werf, G. R. Analysis of daily, monthly, and annual burned area using the fourth-generation global fire emissions database (GFED4). *J. Geophys. Res. Biogeosci*. **2013**, *118*, 317–328.

34. Akagi, S. K.; Yokelson, R. J.; Wiedinmyer, C.; Alvarado, M. J.; Reid, J. S.; Karl, T.; Crounse, J. D.; Wennberg, P. O. Emission factors for open and domestic biomass burning for use in atmospheric models. *Atmos. Chem. Phys.* **2011**, *11*, 4039–4072.

35. Draxler, R. R.; Hess, G. D. An overview of the HYSPLIT_4 modelling system for trajectories, dispersion and deposition. *Aust. Met. Mag.* **1998**, *47*, 295–308.

36. Seibert, P.; Kromp-Kolb, H.; Baltensperger, U.; Jost, D. T.; Schwikowski, M.; Kasper, A.; Puxbaum, H. Trajectory analysis of aerosol measurements at high alpine sites. *Proceedings of the EUROTRAC Symposium* **1994**, 689–693.

37. Wang, Y. Q.; Zhang, X. Y.; Draxler, R. R. TrajStat: GIS-based software that uses various trajectory statistical analysis methods to identify potential sources from long-term air pollution measurement data. Environmental Modelling & Software **2009,** *24*, 938–939.

38. Babu, S. S.; Chaubey, J. P.; Moorthy, K. K.; Gogoi, M. M.; Kompalli, S. K.; Sreekanth, V.; Bagare, S. P.; Bhatt, B. C.; Gaur, V. K.; Prabhu, T. P.; Singh, N. S. High altitude (~4520 m amsl) measurements of black carbon aerosols over western trans-Himalayas: Seasonal heterogeneity and source apportionment. *J. Geophys. Res.* **2011**, *116*, D24201.

39. Kumar, M.; Parmar,K. S.; Kumar, D. B.; Mhawish, A.; Broday, D. M.; Mall, R. K.; Banerjee, T. Long-term aerosol climatology over Indo-Gangetic plain : Trend, prediction and potential source fields. *Atmos. Environ.* **2018**, *180*, 37 – 50.

40. Cheng, I.; Zhang, L.; Blanchard, P.; Dalziel, J.; Tordon, R. Concentration-weighted trajectory approach to identifying potential sources of speciated atmospheric mercury at an urban coastal site in Nova Scotia, Canada. *Atmos. Chem. Phys*. **2013**, *13*, 6031–6048.

41. Guttikunda, S. K.; Jawahar, P. Atmospheric emissions and pollution from the coal-fired thermal powerplants in India. *Atmos. Environ.* **2014**, *92*, 449–460.

42. Reddy, M.; Venkataraman, C. Inventory of aerosol and sulphur dioxide emissions from India: Part II – biomass combustion. *Atmos. Environ*. **2002a**, *36*, 699-712.

43. Reddy, M.; Venkataraman, C. Inventory of aerosol and sulphur dioxide emissions from India: Fossil fuel combustion. *Atmos. Environ*. **2002b**, *36*, 677–697.

44. Dickerson, R. R.; Andreae, M. O.; Campos, T.; Mayol-Bracero, O. L.; Neususess, C.; Streets, D. G. Analysis of black carbon and carbon monoxide observed over the Indian Ocean: Implications for emissions and photochemistry. *J. Geophys. Res*. **2002**, *107*, 8017.

45. Streets, D. G.; Bond, T. C.; Carmichael, G. R.; Fernandes, S. D.; Fu, Q.; He, D.; Klimont, Z.; Nelson, S. M.; Tsai, N. Y.; Wang, M. Q.; Woo, J. H.; Yarber, K. F. An inventory of gaseous and primary aerosol emissions in Asia in the year 2000. *J. Geophys. Res.* **2003**, *108*, 8809.

46. Bond, T. C.; Doherty, S. J.; Fahey, D. W.; Forster, P. M.; Berntsen, T.; DeAngelo, B. J.; Flanner, M. G.; Ghan, S.; Kärcher, B.; Koch, D.; Kinne, S.; Kondo, Y.; Quinn, P. K.; Sarofim, M. C.; Schultz, M. G.; Schulz, M.; Venkataraman, C.; Zhang, H.; Zhang, S.; Bellouin, N.; Guttikunda, S. K.; Hopke, P. K.; Jacobson, M. Z.; Kaiser, J. W.; Klimont, Z.; Lohmann, U.; Schwarz, J. P.; Shindell, D.; Storelvmo, T.; Warren, S. G.; Zender, C. S. Bounding the role of black carbon in the climate system: a scientific assessment. *J. Geophys. Res. Atmos*. **2013**, *118*, 5380–5552.

47. Ohara, T.; Akimoto, H.; Kurokawa, J.; Horii, N.; Yamaji, K.; Yan, X.; Hayasaka, T. An Asian emission inventory of anthropogenic emission sources for the period 1980–2020. *Atmos. Chem. Phys*. **2007**, *7*, 4419–4444.

48. Sahu, S. K.; EIg, G.; Sharma, C. Decadal growth of black carbon emissions in India. *Geophys. Res. Lett*. **2008**, *35*, L02807.

49. Klimont, Z.; Cofala, J.; Xing, J.; Wei, W.; Zhang, C.; Wang, S.; Ke- jun, J.; Bhandari, P.; Mathur, R.; Purohit, P.; Rafaj, P.; Chambers, A.; Amann, M.; Hao, J. Projections of SO_2. NO_x and carbonaceous aerosols emissions in Asia. *Tellus B* **2009**, *61*, 602–617.

50. Lu, Z.; Zhang, Q.; Streets, D.G. Sulfur dioxide and primary carbonaceous aerosol emissions in China and India, 1996-2010. *Atmos. Chem. Phys.* **2011**, *11*, 9839–9864.

51. Pandey, A.; Sadavarte, P.; Rao, A. B.; Venkataraman, C. Trends in multi-pollutant emissions from a technology linked inventory for India: II Residential agricultural and informal industry sectors. *Atmos. Environ.* **2014**, *99*, 341–352.

52. Muhammad, T.; Przemyslaw, J. Electric energy access in Bangladesh. *Transactions on environment and electrical engineering.* **2016**, *2*, 6-17.

53. Bikkina, S.; Sarin, M. M. $PM_{2.5}$, EC and OC in atmospheric outflow from the Indo-Gangetic Plain: Temporal variability and aerosol organic carbon-to-organic mass conversion factor. *Sci. Tot. Environ.* **2014**, *487*, 196.

54. Rengarajan, R.; Sarin, M. M.; Sudheer, A. K. Carbonaceous and inorganic species in atmospheric aerosols during wintertime over urban and high-altitude sites in North India. *J. Geophys. Res.* **2007**, *112*, D21307.

55. Ram, K.; Sarin, M. M.; Tripathi, S. N. A 1 year record of carbonaceous aerosols from an urban site in the Indo-Gangetic Plain: characterization, sources, and temporal variability. *J. Geophys. Res*. **2010b**, *115*, D24313.

56. Rajput, P.; Sarin, M.; Sharma, D.; Singh, D. Characteristics and emission budget of carbonaceous species from post-harvest agricultural-waste burning in source region of the Indo-Gangetic Plain. *Tellus B*, **2014**, *66*.

57. Salam, A.; Bauer, H.; Kassin, K.; Ullah, S. M.; Puxbaum, H. Aerosol chemical characteristics of a mega-city in Southeast Asia (Dhaka-Bangladesh). *Atmos. Environ.* **2003,** *37*, 2517–2528.

58. Tiwari, S.; Srivastava, A.; Bisht, D.; Safai, P.; Parmita, P. Assessment of carbonaceous aerosol over Delhi in the Indo-Gangetic Basin: Characterization, sources and temporal variability. *Nat. Hazards*. **2013**, *65*, 1745–1764.

59. Pachauri, T.; Singla, V.; Satsangi, A.; Lakhani, A.; Kumari, K. M. Characterization of carbonaceous aerosols with special reference to episodic events at Agra, India. *Atmos. Res.* **2013**, *128*, 98–110.

60. Ram, K.; Sarin, M.; Hegde, P. Atmospheric abundances of primary and secondary carbonaceous species at two highaltitude sites in India: sources and temporal variability. *Atmos. Environ.* **2008** , *42*, 6785–6796.

61. Venkataraman, C; Reddy, C. K.; Josson, S.; Reddy, M. S. Aerosol size and chemical characteristics at Mumbai, India, during the INDOEX-IFP (1999). *Atmos. Environ.* **2002**, *36*, 1979–1991.

62. Shubhankar, B.; Ambade, B. Chemical characterization of carbonaceous carbon from industrial and semi urban site of eastern India. *SpringerPlus.* **2016**, *5*, 837.

63. Ram, K.; Sarin, M. M.; Hegde, P. Long-term record of aerosol optical properties and chemical composition from a high-altitude site (Manora Peak) in Central Himalaya. *Atmos Chem. Phys*. **2010a**, *10*, 11791–11803.

64. Rengarajan, R.; Sudheer, A. K.; Sarin, M. M. Wintertime $PM_{2.5}$ and PM_{10} carbonaceous and inorganic constituents from urban site in western India. *Atmos. Res.* **2011**, *102*, 420 – 431.

65. Sandeep, K.; Negi , R. S.; Panicker, A. S.; Gautam, A. S.; Bhist, D. S.; Beig, G.; Murthy, B. S.; Latha, R.; Singh, S.; Das, S. Characteristics and Variability of Carbonaceous Aerosols over a Semi Urban Location in Garhwal Himalayas. *Asia-Pacific J. Atmos. Sci.* **2020**, *56*, 455–465.

66. Ali, K.; Panicker, A. S.; Beig, G.; Srinivas, R.; Acharja, P. Carbonaceous aerosols over Pune and Hyderabad (India) and influence of meteorological factors. *J. Atmos. Chem.* **2016**, *73*, 1–27.